

An Unsupervised Fuzzy System for the Automatic Detection of Candidate Lava Tubes in Radar Sounder Data

Elena Donini¹, Graduate Student Member, IEEE, Leonardo Carrer¹, Member, IEEE, Christopher Gerekos¹, Lorenzo Bruzzone¹, Fellow, IEEE, and Francesca Bovolo¹, Senior Member, IEEE

Abstract—Lava tubes are buried channels that transport thermally insulated lava. Nowadays, lava tubes on the Moon are believed to be empty and thus indicated as potential habitats for humankind. In recent years, several studies investigated possible lava tube locations, considering the gravity anomaly distribution and surficial volcanic features. This article proposes a novel and unsupervised method to map candidate buried empty lava tubes in radar sounder data (radargrams) and extract their physical properties. The approach relies on a model that describes the geometrical and electromagnetic (EM) properties of lava tubes in radargrams. According to this model, reflections in radargrams are automatically detected and analyzed with a fuzzy system to identify those associated with lava tube boundaries and reject the others. The fuzzy rules consider the EM and geometrical properties of lava tubes, and thus, their appearance in radargrams. The proposed method can address the complex task of identifying candidate lava tubes on a large number of radargrams in an automatic, fast, and objective way. The final decision on candidate lava tubes should be taken in postprocessing by expert planetologists. The proposed method is tested on both a real and a simulated data set of radargrams acquired on the Moon by the Lunar Radar Sounder (LRS). Identified candidate lava tubes are processed to extract geometrical parameters, such as the depth and the thickness of the crust (roof).

Index Terms—Fuzzy logic, image processing, lava tubes, radar sounder, subsurface.

I. INTRODUCTION

A LAVA tube is a natural conduit formed beneath the surface that contained thermally insulate lava and transported it over long distances during the active volcanic period [1]. Initially, the basaltic lava streams down from a volcanic vent and streams on the surface similar to

a river. While flowing, the lava develops a continuous thick crust because of the extreme difference of temperature between the hot lava and the outer colder environment [2]. While moving forward, the hard film above the lava continuously congeals, becoming thicker. In this way, a tunnel forms in the subsurface that transports the lava with almost no heat loss [3]. When the lava flows away, the tunnel empties, generating an elongated cavity with a hardened and thick roof. The size and the shape of the tubes strongly depend on the characteristics of lava streams [1]. This phenomenon appears in many bodies of the solar system, including the Earth, Moon, Mars, and Venus. On the Moon and Mars, the volcanic period ended about 50 million years ago [4] and 100–150 million years ago [5], respectively. Hence, lunar and Martian tubes are inactive and expected to be entirely or almost empty, e.g., containing solidified lava or regolith [6]. On the Moon and Mars, hollow and stable tubes can persist for significantly more time than on the Earth because of the colder and drier climate, the weakness of the tectonic activity and weathering rates, and the lower gravity [7]. Moreover, for the same reasons, Martian and lunar lava tubes have larger dimensions than those on the Earth, with widths typically between 10 and 30 m [8]. Hence, terrestrial tubes can be considered as analogs to understanding their formation mechanism and geometrical structure. A lava tunnel network generally consists of the main tube and several smaller ones. It is reasonable to suppose that such networks exist on the Moon and Mars, but there is no specific knowledge on their locations and extension [1]. Also, the characteristics of a single conduit are obscure, e.g., the inner aspect (collapsed, fully or partially filled, hollow), the depth, and the rooftop thickness [9]. However, some studies analyze the possible size range of stable lava tubes on the Moon. Blair *et al.* [10] and Theinat *et al.* [11] simulated tunnels of different dimensions and roof thickness subjected to the lithostatic and the Poisson stress, and the tectonic strain in the subsurface. The results show that stability is correlated with the height of the rooftop and the initial stress state. Lava tubes with a relatively thin roof of 50 m are stable with a width of up to 3.5 km. With a roof thickness of up to 200 m, lava tubes are stable with a maximum width of 5.25 km. Deeper tunnels with a roof thickness of 500 m do not collapse when the width is up to 5 km [10], [11]. The roof thickness is of particular importance for tube stability.

Manuscript received September 17, 2020; revised January 13, 2021 and February 16, 2021; accepted February 24, 2021. This work was supported by the Italian Space Agency through the Attività scientifiche per il radar sounder di EnVision fase A under Contract 2019-25-HH.0. (Corresponding author: Francesca Bovolo.)

Elena Donini is with the Department of Information Engineering and Computer Science, University of Trento, 38123 Trento, Italy, and also with the Center of Digital Society, Fondazione Bruno Kessler, 38123 Trento, Italy.

Leonardo Carrer, Christopher Gerekos, and Lorenzo Bruzzone are with the Department of Information Engineering and Computer Science, University of Trento, 38123 Trento, Italy.

Francesca Bovolo is with the Center of Digital Society, Fondazione Bruno Kessler, 38123 Trento, Italy (e-mail: bovolo@fbk.eu).

Color versions of one or more figures in this article are available at <https://doi.org/10.1109/TGRS.2021.3062753>.

Digital Object Identifier 10.1109/TGRS.2021.3062753

Lava tubes, and more in general subsurface void spaces on the Moon and Mars, have gained an increasing interest in the literature in the past years. First, from a geological point of view, lava tubes are of critical importance as their properties (e.g., the type of minerals and rocks and the elongation) can help in understanding the geological evolution. Second, lava tubes are the perfect places for building structures for living, storing food, and electronics [12]–[14]. Third, several works identified subsurface cavities as the perfect place where humankind can safely settle sheltered from the threats on the surface [15], [16]. The roof of the tube acts as a shelter against surficial threats, e.g., cosmic and solar radiations and Gamma rays [2], [12], [17], the extreme temperature variation [12], the regolith small and toxic dust, and the frequent meteoritic impacts. Finally, as the surface is a hostile environment, buried cavities may store water and may be a stable physical and chemical environment that preserves microbial biosignature, as an analogy to the Earth [18], [19].

Lava tubes can hardly be mapped with direct measurements, especially on the Moon, Mars, and isolated places on the Earth. On Earth, lava tubes are mapped and studied on-site, which is not possible in space. There exist four main strategies for mapping lava tubes 1) employing optical and synthetic aperture radar (SAR) images to identify surface volcanic features linked to subsurface cavities [2], [20]–[24]; 2) studying skylights from oblique views in images acquired at different wavelengths [14], [25]; 3) detecting distribution anomalies in the gravity data that may correspond to subsurface mass deficits [26]; and 4) analyzing radar sounder data [1], [9], [27]. The first approach investigates geological volcanic structures on the surface that are correlated with buried lava tubes, i.e., rilles [2], [20]–[22] and huge pits [23]. These structures can be interpreted as locally collapsed lava tubes because of preexisting fractures in the roof, meteoric impacts, or a thin roof unable to sustain the tube weight. Note that the subsurface void should be large enough to contain the crust material, especially for pits in a chain formation. The second approach analyzes the differences between impact crater holes and skylights at visible and thermal wavelengths with several angles of incidence [14], [25]. At visible wavelength, skylights lack any impact crater properties (e.g., raised rims and ejected patterns). At infrared wavelength, during the day inside the skylights, the temperature fluctuates less widely than in the nearby surface and adjacent bowl-shaped pit craters. At nighttime, the pit floor shows a higher temperature than in the surrounding pits, which suggests the presence of an extended subsurface cavity mitigating the fluctuation [14]. The third strategy analyzes anomalies in the gravity distribution to identify mass deficits that can be compatible with hollow lava tubes. Chappaz *et al.* [26] estimated the subsurface density and detected buried cavities by exploiting negative anomalies, i.e., lower density values. The fourth strategy analyzes radar sounder and ground-penetrating radar (GPR) data as they provide a direct measure of the subsurface. Investigating GPR data, Miyamoto *et al.* [1] and Rowell *et al.* [9] mapped and characterized complex networks of lava tubes. Rowell *et al.* [9] proposed a method to detect the pattern of lava tubes that exploits *a priori* knowledge of the tunnel connections and

geometries, e.g., the tube dimensions and roof thickness. However, this knowledge is not always available for terrestrial nor planetary cases. Miyamoto *et al.* [1] proposed an approach to detect lava tubes by analyzing the vertical profiles of radargrams (A-scan). A-scans were compared with a specific pattern characterized by two high peaks, compatible with the expected lava tube behavior. The same approach was applied to radargrams of the Moon aiming at mapping the tunnel network [27]. However, in both studies, each a-scan is separately analyzed without checking the peak spatial correlation or extracting information on the tube dimension. Note that peaks do not uniquely represent lava tubes but any strong reflections in the subsurface, such as clutter. Recently, a new strategy was proposed to detect possible lava tubes [27] for discriminating between clutter and subsurface reflections [28]. The strategy is based on three criteria: 1) analysis of multiple orbit data (if available); 2) evaluation of the correlation between radargrams and surface scattering simulations; and 3) analysis of the surface slope echo. However, radar sounder data store more information that can be used to identify buried geological structures and understand the processes in the subsurface. Radar sounders are active sensors that can probe the subsurface in a nonintrusive way and, thus, without digging nor coming in contact with the observed body. They transmit in the nadir direction electromagnetic (EM) waves that can penetrate the surface and propagate in the subsurface. The signal has a low frequency in the range of high frequency (3–30 MHz) or very high frequency (30–300 MHz) and relatively wide bandwidth up to 100 MHz depending on the central frequency. The radar waves measure the subsurface structures because of the different dielectric properties. They interact with the EM signal, generating reflected echoes collected by the antenna. These echoes are coherently summed together and contain in radargrams. Analyzing radargram is possible to extract significant information on the subsurface structures and processes [29]–[32], not retrievable with the other approaches.

This article proposes a novel automatic method to detect reflections from candidate cavities, such as empty and buried lava tubes, in radar sounder data. The method, which extends and develops the initial idea in [30], is unsupervised (does not require a training phase), considers the intrinsic nature of the lava tubes in the subsurface, and is flexible. It consists of three main concepts: 1) the EM modeling of the lava tube signature in the radargrams; 2) extracting reflections in the radargram; and 3) analyzing the reflections to identify those related to candidate lava tubes. The EM modeling describes how lava tubes appear in radargrams by analyzing the interaction between the propagating EM wave and the buried cavities, seen as the transition rock-void-rock in the subsurface. Considering the lava tube model, the method extracts reflections in radargrams and then analyzes them to identify those related to buried cavities and reject the others. The analysis consists of a fuzzy detection system based on the lava tube EM model that evaluates the reflection properties and their relation. The proposed method identifies candidate lava tubes in an automatic, fast, and objective way. Given the complexity of the task, this is not feasible with visual analysis on a large number of radargrams. The final decision

on the identified candidate lava tubes should be made in the postprocessing by expert planetologists. The effectiveness of the proposed method is demonstrated with experiments on two data sets: a data set of simulated radargrams and a data set of radargrams acquired on the Moon by the Lunar Radar Sounder (LRS).

This article is organized as follows. Section II presents the geological and EM models for lava tubes. Section III focuses on the method proposed to detect lava tubes by describing the algorithm to extract the reflection from the radargram and the fuzzy system that analyzes the reflections to identify lava tubes. Section IV is devoted to describing the two data sets and the experimental results. Section V discusses the limitations and the assumption of the proposed method. Finally, Section VI presents the conclusions and future work.

II. LAVA TUBE MODEL

Lava tubes are tunnel-like structures that drain over time, generating elongated buried cavities. The void and the rock have highly different dielectric properties, which make the interfaces between the two materials detectable by radar sounders. In radargrams, interfaces appear as strong reflections with specific characteristics in amplitude and phase. This section describes the EM and geometrical model of lava tubes in terms of reflections generated by the surface and the lava tube boundaries. To investigate the properties of these reflections, we simulated the amplitude and phase radargrams with a coherent multilayer simulator [33]. The simulator takes as input the parameters of the radar EM wave (e.g., the central frequency, the bandwidth, and the modulation of the carrier signal). Moreover, the simulator allows choosing the crossing angle α between the moving direction of the radar platform and the lava tube longitudinal axis. Finally, the simulator requires the geometrical and dielectric models of the surface and the subsurface. It considers the surface topography (e.g., roughness and craters), the geometry of the buried geologic structures, and the dielectric properties of the materials. Here, we first simulate an ideal scenario where above the surface is void, and the rocky subsurface contains an empty lava tube. The simulations consider the geometric model of planetary lava tubes in [10] and [34]. The lava tube geometrical model considers stable structures with the tunnel sizes and the roof thicknesses shown in Table I that follows the analyses in [10] and [34]. The tunnels are approximated as half-cylinders with a height-to-width ratio of 1:3, i.e., the tube height is one-third of the tube width, as in [10]. For the dielectric model, we consider the ideal case with the void in the tube, which is characterized by a unitary relative dielectric constant $\varepsilon_r^{\text{void}} = 1$. Note that in real scenarios, the lava tube inside can be partially filled by regolith or other materials having a lower dielectric constant than that of the rock. The basaltic rock around the conduit is approximated by a relative dielectric constant of $\varepsilon_r^{\text{rock}} = 4$ and a loss tangent of $\delta_{\text{rock}} = 0.01$. Considering the lunar scenario, at the simulation central frequency f_c , the dielectric constant of the surface ε_r varies from 4 up to 8 and the upper limit of the tangent loss δ is in the range of 0.1–0.3 [35]. Hence,

TABLE I
PARAMETERS OF THE GEOMETRICAL MODEL OF THE SIMULATED LAVA TUBE, CONSIDERING THE STABLE SCENARIO [10], [34]. NOTE THAT THE TUBE HEIGHT IS ASSUMED TO BE ONE THIRD OF THE TUBE WIDTH

Frequency	Bandwidth	Tube Width	Roof Thickness	Tube Size
10 MHz	5 MHz	250 m	5 m	small
10 MHz	5 MHz	625 m	50 m	
60 MHz	30 MHz	1000 m	75 m	average
10 MHz	5 MHz	1000 m	130 m	
10 MHz	5 MHz	1250 m	20 m	
10 MHz	5 MHz	1500 m	20 m	
10 MHz	5 MHz	2000 m	200 m	large
10 MHz	5 MHz	4000 m	200 m	
10 MHz	5 MHz	3000 m	200 m	

TABLE II
RADAR PARAMETERS OF THE SIMULATIONS AND THE LRS [38], AND RESOLUTION PARAMETERS OF THE RADARGRAMS

Parameter	Simulations	LRS [38]
Orbit altitude	100 Km	100 Km
Central frequency	10-60 MHz	5 MHz
Bandwidth	5-30 MHz	2 MHz
Sampling time	0.17 μs	0.16 μs
Maximum penetration depth	7.5 Km	5 Km
Azimuth resolution	5 m	60 m
Range resolution in free space (pulse compressed)	15 m	75 m

simulations refer to the worst case scenario in terms of surface dielectric properties. Recently, a study [36] showed that in the frequency range of 10–100 MHz, the regolith absorption and volume scattering are negligible. Thus, the EM wave is affected only by losses due to the surface roughness, i.e., the topography. The attenuation depends on the loss tangent and mainly affects the reflections from the lava tube rather than from the surface. Considering a loss tangent and a dielectric constant at the ceiling and floor of the tube equal to that of the surface, the maximum detectable depth of lava tubes strongly depends on f_c [36]. At frequencies in the range of 60–100 MHz, it is in the range of some hundred meters and it increases as f_c decreases [36]. For the signal modulation, the EM wave has a chirp waveform smoothed by a Hann window [37]. We simulated signals by varying central frequencies, transmitted power, and height of the radar from the surface, as shown in Table II. For the crossing angle α , we simulated the cases in the range of $\alpha \in (0, \pi/2)$. The two extreme cases are: 1) $\alpha = 0$, which represents the tube axis being parallel to the moving direction of the radar, and 2) $\alpha = \pi/2$, which models the tube axis being perpendicular to the moving direction of the radar. Fig. 1(a) and (b) shows the tube in yellow and the moving direction of the radar in red for $\alpha = 0$ and $\alpha = \pi/2$, respectively. Regarding the topography of the surface, we first considered an ideal and flat surface to focus on the reflections due to the lava tubes. Then, we simulated a more complex and realistic topography

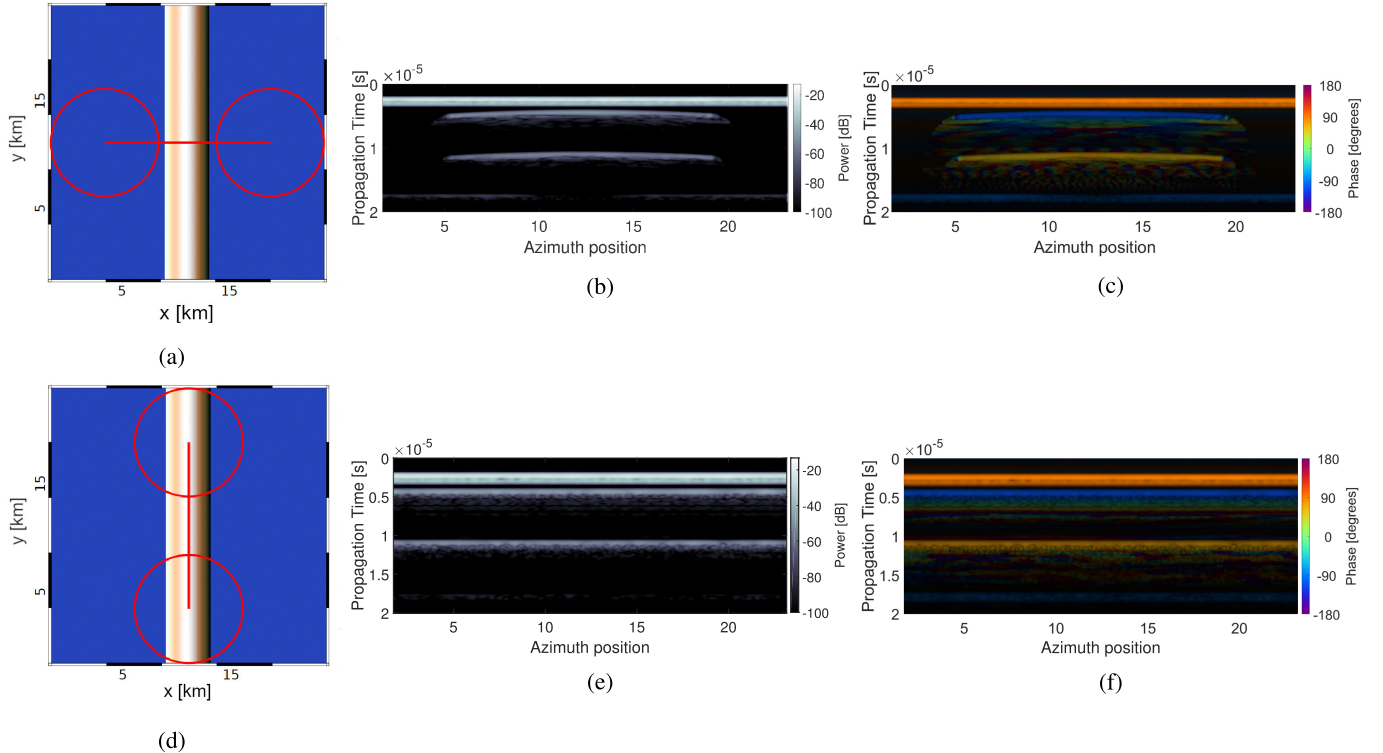


Fig. 1. Simulated amplitude and phase radargrams of a lava tube with deep $d = 200$ m and diameter $2r = 4$ km for the cases $\alpha = \pi/2$ and $\alpha = 0$. (a) and (d) Track of the direction of the radar and the tube axis (both in red) with an angle $\alpha = \pi/2$ and $\alpha = 0$, respectively. (b) and (c) Simulated amplitude and phase radargrams for the perpendicular case, respectively. (e) and (f) Simulated amplitude and phase radargrams for the parallel case, respectively.

to analyze how the surficial clutter interacts with the pattern of lava tubes. Considering such a scenario, here, we describe the EM model of lava tubes from the amplitude and phase point of view.

A. Lava Tube Amplitude Model

The amplitude radargram shows three strong and linear reflections that represent the surface, the ceiling, and the floor of the tube (see Fig. 1). The surface reflection (G) ideally appears as a bright line as long as the radargram with the greatest amplitude. This reflection is the first interface that the radar wave encounters. The tube generates a pattern made of a couple of reflections that represent the two interfaces between the void and the basaltic rock. The upper reflection (C) is generated by the ceiling of the tube, whereas the lower one (F) is generated by the floor. The amplitudes a_C and a_F are smaller than that of the surface but similar to each other. The distance between the reflections in the range direction is proportional to the depth of the interfaces. The reflection lengths (l_C , l_F) along the azimuth depend on the size of the tube and the crossing angle α . Concerning the angle α of intersection between the tube axis and the flight track of the sounder, there are two limit cases: $\alpha = 0$ and $\alpha = \pi/2$. When $\alpha = 0$ [parallel case, see Fig. 1(d)–(f)], the couple of reflections is ideally as long as the radargram in azimuth [see Fig. 1(e)]. Note that the reflection length depends on the acquisition—a radargram may image part of the lava tube or cover a wider area than that of the tube. When $\alpha = \pi/2$ [perpendicular case, see Fig. 1(a)–(c)], the reflection lengths (l_C , l_F) are similar and shorter than

the radargram in azimuth [see Fig. 1(b)]. Smoothly moving from the latter to the former case, the reflections preserve the (almost) linear shape stretching until the parallel case.

B. Lava Tube Phase Model

In the phase domain, the lava tube model has three reflections with the same length and depth (i.e., range position) as in the amplitude domain. The main property of the phase model is the phase inversion [36] of the reflections originating from the lava tube ceiling when compared to the surface reflection. This effect on the radar signal is expected from a dielectric discontinuity where the first medium has a higher permittivity than the second one. In our case, the first medium is basalt, whereas the latter is the vacuum, modeling the lava tube's inner free space. The lava tube floor is expected to have the same phase sign as the surface reflection.

The above-mentioned amplitude and phase models assume an ideal scenario with flat topography, i.e., a plane and roughness-free surface. In this scenario, we identify the reflection pattern of empty tubes without the presence of clutter. We further investigate more realistic scenarios with complex surface topography. To this end, we introduce sharp roughness and deep craters to verify the impact of the surface clutter on the reflection pattern of the tubes (see Fig. 2). The simulations indicate that craters generate clutter reflections with a pattern similar to that of the lava tubes in amplitude but not in phase. The lava tube models are not affected by significant changes, i.e., the three reflections maintain the main properties

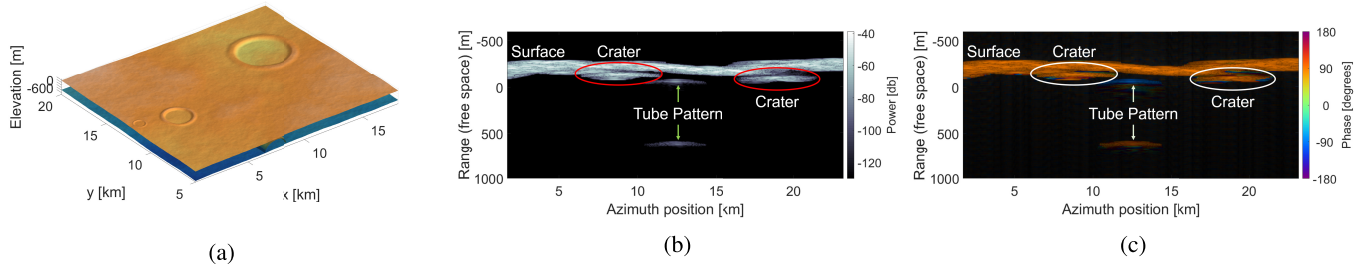


Fig. 2. (a) Surface terrain is characterized by a high rough surface and thick craters. (b) Simulated amplitude and (c) phase radargrams of a lava tube with deep $d = 200$ m and diameter $2r = 4$ km for the case $\alpha = \pi/2$. Reflections generated by the surface, the craters, and the lava tube ceiling and floor are highlighted in radargrams [see (b) and (c)].

described above. The model preserves the inversion of the phase at interfaces of materials with considerably different dielectric constants. The surface reflection G is affected by the volume scattering due to the roughness and clutter signals. The rim and the ground of the craters create several clutter signals above and below the surface. However, the crater reflections do not have phase inversion and, thus, are distinguishable from those of the tube boundaries (see Fig. 2). Regarding the pattern of lava tubes, C and F maintain the properties of the phase model. In amplitude, the ceiling and the floor reflections show a loss of about 5 dB, which is confirmed in [27] and [36]. In a more realistic scenario, lava tubes are not perfect cylindrical bodies but have a more complex geometrical shape [39]. The profile of lava tubes is typically characterized by a flat and extended floor and shorter and sharper ceiling. Moreover, lava tubes are not straight and parallel to the surface, but they have a sinuous track and may have an inclination toward the surface. This geometry is reflected in the shape and position of C and F : 1) C and F are not expected to be perfectly parallel between them and with the surface and 2) C and F may not share the same length and may not fully overlap in the azimuth direction. However, the lava tube pattern is still distinguishable because of the phase inversion between C and F . Finally, recent studies show that the tube may be filled with regolith [1] or other media having dielectric properties similar to that of the void. Thus, the EM model for the lava tube is still valid as the large difference in the dielectric properties of the media produces a phase inversion.

III. PROPOSED APPROACH TO DETECT CANDIDATE LAVA TUBES

Let us consider a radargram as a 2-D matrix of n_T traces and n_S samples

$$\mathbf{R} = \{R(x, y) | x \in X = [1, \dots, n_T], y \in Y = [1, \dots, n_S]\} \quad (1)$$

where R is the coherent sum of the echoes stored in the radargrams and x and y indicate the range and the azimuth coordinates, respectively. The radargrams contain the complex signal reflected from the interfaces between different media in the subsurface such that $R(x, y) = R_R(x, y) + jR_I(x, y)$, where $R_R(x, y)$ is the real part of the signal and $R_I(x, y)$ the imaginary part. The amplitude $A(x, y)$ and

phase $\Phi(x, y)$ radargrams are defined as follows:

$$\begin{aligned} A(x, y) &= \sqrt{R_R^2(x, y) + R_I^2(x, y)} \\ \Phi(x, y) &= \arctan \frac{R_I(x, y)}{R_R(x, y)}. \end{aligned} \quad (2)$$

Let $\mathcal{F} = \{\mathbf{F}_i, i \in [1, \dots, N_F]\}$ be the set of features extracted from the radargram, where F_i indicates the i th feature, i.e., the coordinates of the pixels of the reflection in the radargram and the related properties. The proposed approach assigns to each feature a class in $\Omega_c = \{\omega_g, \omega_c, \omega_f, \omega_n\}$. ω_g indicates the best candidate to represent the surface, and ω_c and ω_f indicate features that can be generated by the candidate tube boundaries (the ceiling and the floor, respectively). ω_n labels features that are related neither to buried cavities nor to the surface but probably generated by the surface topography and other volcanic structures, e.g., impact craters, tesserae, and off-nadir clutter.

A novel automatic technique is proposed with three steps (see Fig. 3):

- 1) extraction of the coordinate of the reflections in the radargram;
- 2) extraction of the properties of each reflection to define the feature set;
- 3) analysis of the features to detect those generated by the surface and candidate lava tube boundaries, exploiting the model in Section II.

According to the analysis in Section II, the properties of the lava tube EM model are the following.

- 1) There should be at least one candidate surface reflection having the shallowest depth in the range and the greatest power return.
- 2) There should be at least two other deeper reflections, i.e., the candidates for the boundaries of the lava tube C and F .
- 3) The reflection length depends on the tube width and the crossing angle α between the tube axis and the moving direction of the radar.
- 4) Candidate features for the same tube should have as similar as possible length, independent of the crossing angle α .
- 5) There should be alignment between the candidate features C and F , i.e., the barycenters of the candidate C and F should lie on the same line.
- 6) Phase inversion should occur at ceiling candidate feature.

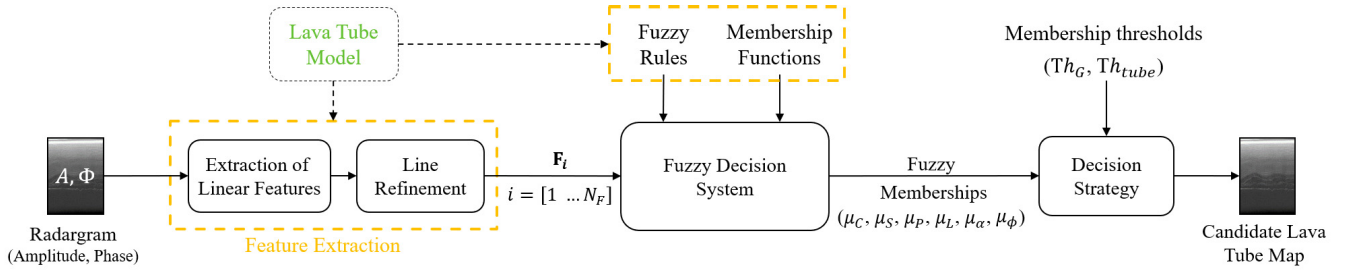


Fig. 3. Flowchart of the proposed approach to detect candidate lava tubes.

Note that candidate features in the radargrams will have different characteristics, including thickness, shape, and orientation according to the acquisition geometry, the resolution in the range direction (which also depends on the specific dielectric properties of the medium), and the physical properties of the geological structures. Furthermore, real radargrams usually present other reflections related to undesired signals, such as clutter from off-nadir and surface topography variations. Hence, the automatic system to detect lava tube reflections must be robust to noise and uncertainties in radargrams, given by the impossibility of precisely modeling the subsurface structures.

A. Detection of the Reflections

Considering the model presented in Section II, the signature of both the lava tube boundaries and the surface consists of reflections with a linear shape. Hence, the first step of the proposed approach extracts the candidate features with a line detection algorithm. In the literature, there exist several methods to detect lines in radargrams, such as [31] and [32]. Here, we used the unsupervised method in [31] that can extract lines with different properties, e.g., orientation, shape, and length. Furthermore, the method is robust to both the thermal and background noise of radargrams. The algorithm [31] automatically detects lines in radargrams by applying a local scale hidden Markov model (HMM) and the Viterbi algorithm (VA). The overall approach consists of the following steps: 1) layers enhancement; 2) segment detection using a combination of the VA and HM model in small regions of the radargram; and 3) combination of adjacent segments. (See Fig. 4 for the schematic representation). The HMM detects the most probable location of the lines and transforms the pixels in these regions into a graph. The VA analyzes the graphs to identify the pixels belonging to the lines. The approach divides radargrams into small portions processed separately. Then, a detection strategy links inferred local segments.

The initial step enhances the signal while reducing the noise in the radargram with an incoherent averaging filter that magnifies locally flat lines with a size of N_{AV} (reflections that are flat at least at the scale of the averaging length). Then, the algorithm adaptively estimates the conditional density function (CDF) of the noise and the signal. Knowing these CDFs and fixing the probability of false alarm, the algorithm computes the probability of detection and the peak threshold. The peak threshold is applied to each rangeline (a column of the radargram) to detect the local peaks, potentially associated

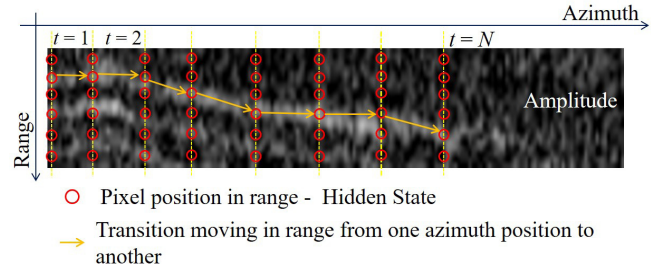


Fig. 4. Illustration of the tracking procedure of a single layer edge. The pixels with the red circle connected by the yellow arrow identifies a retrieved best path.

with lines. Since reflections are spread in range, i.e., they are some pixels thick, the algorithm considers only peaks separated by at least a unit of range resolution (skeleton thickness) to avoid multiple detections of the same reflection.

The second step applies the HHM and the VA to detect the lines. HHM transforms the radargram into a graph where the VA searches for the optimal state sequence. For each azimuth position, the VA considers as initial seeds the previously detected peaks. Then, it iteratively identifies the optimal state sequence in the radargram portion surrounding the seeding points. The amplitude of the pixels in the best path is thresholded Th_{line} to check whether the path is related to a reflection. Then, the algorithm connects the line of adjacent radargram portions in a way that the initial seeds of the next portion are the last pixels of the best paths of the previous block. The algorithm stops when it reaches the end of the radargram or when the thresholding condition is no longer verified. When a line is detected, the corresponding pixels are removed from the radargram to avoid multiple detections.

The algorithm extracts a set of lines $\mathcal{L} = \{\mathbf{L}_k, k \in [1, \dots, N_L]\}$ corresponding to high reflection values in the radargram. For each line, the algorithm provides the azimuth a and range r coordinates for each pixel. The algorithm extracts many segments for each reflection as it is sensitive to the amplitude variations. Hence, a step of postprocessing combines segments related to the same reflection. Segments shorter than L_{min} are removed as they are expected to represent noise or unwanted reflections. Segments are grouped by considering the relative distances in the azimuth and range. Two segments are grouped if: 1) they overlap in the azimuth or the range directions of O_a and O_r pixels and 2) the amplitude of the edge connecting the two lines is constant and higher than the threshold Th_{line} . The first condition identifies the candidate segments

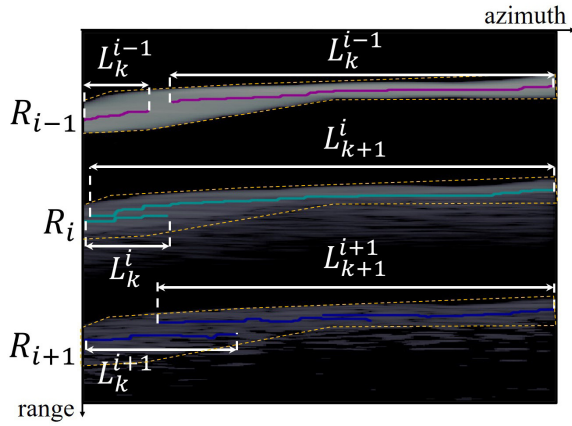


Fig. 5. Examples of the refinement step: several segments \mathbf{L}_k^i are extracted for each reflection \mathbf{R}_i .

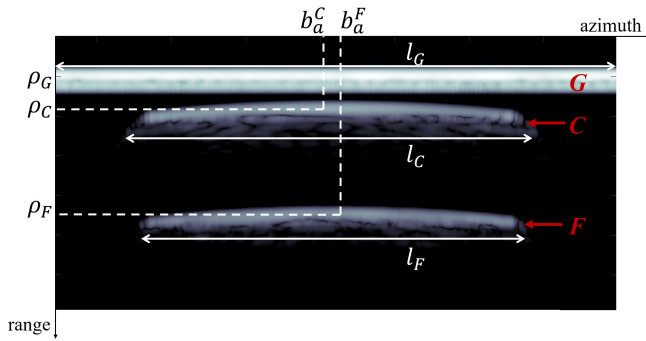


Fig. 6. Simulated radargram imaging the surface reflection G , the tube ceiling C , and the floor F with the main geometrical parameters for each i th reflection (length l_i , average depth ρ_i , and azimuth barycenter coordinate b_a^i).

to combine. The second one combines only the segments that are likely to represent the same reflection. The output of this step is a set of reflections $\mathcal{R} = \{\mathbf{R}_i, i \in [1, \dots, N_R]\}$, where the i th reflection groups several segments \mathbf{L}_k^i . (See Fig. 5 for a schematic representation). For each reflection, a geometrical region is built by considering as starting and ending point the coordinates of the most left and most right pixel of each line group.

B. Characterization of the Reflections

The second step of the proposed approach characterizes the i th reflection by extracting the length l_i , the average depth ρ_i , the barycenter coordinates b_i , the average amplitude a_i , and the average phase ϕ_i (see Fig. 6). These parameters compose a feature vector $\mathbf{F}_i = \{l_i, \rho_i, b_i, a_i, \phi_i\}$ for each reflection \mathbf{R}_i .

1) *Length*: For each reflection \mathbf{R}_i , the length l_i considers the extension in the azimuth direction of the reflection with

$$l_i = \max \{l_a^k\} - \min \{l_a^k\}, \quad k \in [1 \dots N_L^i] \quad (3)$$

where l_a^k is an array indicating the azimuth coordinates of the k th line and N_L^i is the number of segments of the i th reflection. The reflection length is equal to the distance between the points with the lowest and the highest azimuth coordinate. This considers the distance between the two extreme points, without considering the overlapping of the lines in the azimuth.

2) *Depth*: The average depth ρ_i considers the average range coordinate of each reflection according to

$$\rho_i = \frac{\max \{l_r^k\} + \min \{l_r^k\}}{2}, \quad k \in [1 \dots N_L^i] \quad (4)$$

where l_r^k is the array of the range coordinates of the k th line of the i th reflection. The average depth of the reflection is equal to the midpoint between the lowest and the highest range coordinate. This considers the reflection thickness but not the overlapping of the lines in the range direction.

3) *Barycenter*: The barycenter b_i is calculated by considering the centroid of the geometrical region of each reflection. Hence, the azimuth b_a^i coordinate of the centroid is calculated as follows:

$$b_a^i = \frac{\max \{l_a^k\} + \min \{l_a^k\}}{2}, \quad k \in [1 \dots N_L^i] \quad (5)$$

whereas the range coordinate is equal to the average depth of the feature $b_r^i = \rho_i$.

4) *Amplitude*: The average amplitude a_i of each reflection is considered as the average amplitude of the pixels belonging to the N_L^i lines of the i th reflection. Hence, the average amplitude is computed as follows:

$$a_i = \text{mean} \{A(l_a^k, l_r^k)\}, \quad k \in [1 \dots N_L^i] \quad (6)$$

where $A(l_a^i, l_r^i)$ is the amplitude radargram at the azimuth and range coordinates of the lines in the i th reflection.

5) *Phase*: The last parameter is the average phase ϕ_i related to the change of media in the propagation path of the EM wave. The phase radargrams store the phase signal that depends on: 1) the interactions between the EM wave and the medium where it propagates and 2) the length of the path traveled by the EM wave. Here, the aim is to identify the phase shift due to the interaction between the EM wave and the subsurface structures and media. The phase shift can be estimated as the difference in the length of the traveled path and the total phase value. To this end, for each reflection, the phase value of each pixel is computed by analyzing the signal properties in the frequency domain. Let us consider the i th reflection to define the strategy to extract the average phase value from the phase radargram. In the amplitude domain, the range coordinate of the signal peak r_p^i is identified for each column of the geometric region. In the phase domain, the p th column of the geometrical region is convolved with a Hann window $W_{\text{hann}}(y)$ centered in the peak in the following equation:

$$W_{\text{hann}}(y) = \begin{cases} \frac{1}{2} \left(1 + \cos \left(\frac{2\pi r_p^i}{T} \right) \right), & |r_p^i| \leq T/2 \\ 0, & |r_p^i| > T/2 \end{cases} \quad (7)$$

where r_p^i is the range coordinate of the peak in the p th column of the geometrical region of the i th reflection and T is the length of the considered surrounding window. In the frequency domain, the Hann window has low aliasing, low sidelobes, and a narrow main lobe. These properties limit the impact of the filtering on the phase signal while having an accurate selection of the frequency and a low level of signal distortions. Then, the output of the convolution is transformed into the frequency

domain by applying the Fourier transformation (FT). In the frequency domain, the signal is complex and the phase can be estimated by calculating the angle of the signal. Hence, the average phase value θ_i for the i th reflection is the average of the phase computed for each range line. Note that θ_i is the phase value having the contributions from the length of the EM wave propagation path θ_i^{path} and the interaction of the wave with the material ϕ_i . ϕ_i can be estimated with $\phi_i = \theta_i - \theta_i^{\text{path}}$, where θ_i^{path} is defined by setting $y = \rho_i$ in the following equation:

$$\theta_i^{\text{path}}(y) = \frac{4\pi}{\lambda}[\rho(y) + h]\sqrt{\varepsilon_r(y)} \quad (8)$$

where λ is the wavelength of the signal, h is the elevation of the radar, and $\varepsilon_r(y)$ is the relative permittivity of the propagation medium, which depends on the range. Note that $\rho_i + h$ is the length of the propagation path of the EM wave from the radar to the interface in the subsurface. $\varepsilon_r(y)$ indicates the propagation medium; here, the dielectric profile considers basaltic rock $\varepsilon_r^{\text{rock}}$ in the subsurface, and vacuum in the buried cavities and above the surface. Once the phase contribution given by the propagation path is calculated, the phase shift from the change of dielectric properties in the medium can be estimated. Note that the lava tube model considers the phase inversion between a couple of reflections, such as the reflection from the cavity boundaries. Once the candidate features to be the surface and the tube boundaries are identified, the relative phase between the reflections can be computed. The phase signal of the candidate to be the surface, and the tube ceiling and floor are estimated in (9), as the difference between the phase contribution from the propagation path of the EM wave and that of the dielectric properties

$$\begin{aligned} \Phi_G &= \frac{4\pi h}{\lambda} \sqrt{\varepsilon_r(\rho_G)} \\ \Phi_C &= \frac{4\pi h}{\lambda} \sqrt{\varepsilon_r(\rho_G)} + \frac{4\pi(\rho_C - \rho_G)}{\lambda} \sqrt{\varepsilon_r(\rho_C)} + \phi_C \\ \Phi_F &= \frac{4\pi h}{\lambda} \sqrt{\varepsilon_r(\rho_G)} + \frac{4\pi(\rho_F - \rho_G)}{\lambda} \sqrt{\varepsilon_r(\rho_F)} + \phi_F \end{aligned} \quad (9)$$

where ρ_G , ρ_C , and ρ_F are the average depth of the ground reflection G , ceiling reflection C , and floor reflection F , respectively. $\rho_C - \rho_G$ is the roof thickness (the propagation path of the EM wave from the surface to cavity ceiling), while ϕ_C is the phase contribution given by the change of dielectric properties of the material at the tube ceiling. $\rho_F - \rho_G$ is the propagation path from the surface to the floor of the cavity (sum of the roof thickness and the tube height), while ϕ_F is the phase contribution given by the change in the dielectric properties of the material at the tube floor. Finally, the dielectric properties $\varepsilon_r(y)$ depend on the dielectric profile and, thus, the depth. Comparing the phase of two reflections, we can check the phase inversion as the difference between the phases of the two candidate features

$$\begin{aligned} \Phi_C - \Phi_G &= \frac{4\pi(\rho_C - \rho_G)}{\lambda} \sqrt{\varepsilon_r(\rho_C)} + \phi_C \\ \Phi_F - \Phi_C &= \frac{4\pi(\rho_F - \rho_C)}{\lambda} \sqrt{\varepsilon_r^{\text{tube}}} + \phi_F - \phi_C. \end{aligned} \quad (10)$$

The first part of both equations is related to the phase signal due to the propagation path, whereas the latter is from the dielectric properties of the medium. In the first equation of (10), the wave propagates into the lava tube roof, which consists of basaltic rock. In the second equation of (10), the wave propagates in the tube that generally is void and has a relative permittivity $\varepsilon_r^{\text{tube}} = \varepsilon_0 = 1$. The phase contribution from the materials ϕ_C and ϕ_F is the unknown of the equation that can be estimated by inverting (10). Note that according to the lava tube EM model, $|\phi_C|$ is ideally equal to π since a phase inversion occurs when moving from the rock to the void of the tube. Hence, the phase difference depends on the unknowns ($\varepsilon_r^{\text{tube}}$, ϕ_C , and ϕ_F) and allows us to derive the phase shift.

C. Fuzzy Detection Approach

This section focuses on the proposed strategy to analyze the set of features $F = \{\mathbf{F}_i, i \in [1, \dots, N_F]\}$ extracted from the radargram with a fuzzy logic-based system. The system examines the properties of the features ($\mathbf{F}_i = \{l_i, \rho_i, b_i, a_i, \phi_i\}$) and assigns to each of them a label in $\Omega_c = \{\omega_g, \omega_c, \omega_f, \omega_n\}$. The fuzzy logic models the uncertainty of the lava tube EM model in the realistic scenario and accounts for the characteristics of the data, such as their low resolution. The fuzzy system consists of two steps: 1) the best candidate feature to be the surface reflection is identified and removed from the feature set and 2) the remaining features are analyzed two-by-two to detect the couples of features that can be candidates to be the lava tube ceiling and floor. When two features are identified as possible reflection generated by the lava tube boundaries, these are removed from F to avoid multiple detections of the same cavity. The analysis of the features is done with a set of rules (see Table III) based on the EM model presented in Section II. Each rule evaluates the features by providing a membership value in the range of $[0, 1]$. This value indicates how much that rule is fulfilled, i.e., a high membership value indicates that the rule is verified for that feature, whereas a low value indicates the contrary.

The first step aims at detecting the best candidate feature to represent the reflection generated by the ground surface among the candidate features $\mathbf{F}_i, i \in [1 \dots N_F]$. Ideally, the surface reflection has a length comparable to that of the radargram in azimuth. Furthermore, it has the smallest average range coordinate since it is the first interface encountered by the wave. To identify the surface reflection, two fuzzy rules described below evaluate the candidate features and associate a grade of membership to all of them. According to the overall membership value, the best candidate to represent the surface reflection is detected.

1) *Completeness*: Three reflections generated from the surface and the tube ceiling and floor must be detected in the radargram to identify a possible candidate. This rule evaluates the presence of at least three features such that $\mathbf{F}_i, i \in [1 \dots N_F], N_F \geq 3$. Fixing the parameter $p = N_F$, p is evaluated with a crisp membership function $\mu_C(p)$, defined as $\mu_C(p) = [0, 1]$. The function analyzes the number of features N_i and is $\mu_C(p) = 1$ when three or more reflections are detected; otherwise, it is $\mu_C(p) = 0$.

TABLE III
SUMMARY OF THE FUZZY RULES USED TO CLASSIFY EACH FEATURE AS POSSIBLE SURFACE REFLECTION ω_g ,
LAVA TUBE CEILING REFLECTION ω_c , LAVA TUBE FLOOR REFLECTION ω_f , AND NONE OF THEM ω_n

Rule	Attribute	Membership Function
1. Presence of at least 3 candidate features F_c , F_f , and F_g (completeness)	p	$\mu_p(p) = \{0, 1\}$
2. Surface length of the candidate feature F_g	$r_G = \frac{l_g}{l_R}$	$\mu_G(r_G) = \frac{1}{1 + \exp(-a_G(r_G - c_G))}$
3. Equivalence of length of the candidate features F_c and F_f	$r_L = \min\{\frac{l_c}{l_f}, \frac{l_f}{l_c}\}$	$\mu_L(r_L) = \frac{1}{1 + \exp(-a_L(r_L - c_L))}$
4. Proportionality of the candidate features F_c and F_f	$r_P = \min\{\frac{l_c}{l_f}, \frac{l_f}{l_c}\}$	$\mu_P(r_P) = \frac{1}{1 + \exp(-a_P(r_P - c_P))}$
5. Alignment of the barycenters of the candidate features F_c and F_f	$r_{al} = m - mal $	$\mu_{al}(r_{al}) = \frac{1}{1 + \exp(-a_{al}(r_{al} - c_{al}))}$
6. Comparison of the amplitude values of the candidate features F_c and F_f	$r_A = \min\{\frac{a_c}{a_f}, \frac{a_f}{a_c}\}$	$\mu_A(r_A) = \frac{1}{1 + \exp(-a_A(r_A - c_A))}$
7. Phase inversion between the candidate features F_c and F_f	$r_\phi^1 = \min\{ \frac{\phi_c}{\pi} ; \frac{\pi}{\phi_c} \}$	$\mu_\phi^1(r_\phi^1) = \frac{1}{1 + \exp(-a_\phi^1(r_\phi^1 - c_\phi^1))}$
	$r_\phi^2 = \min\{ \frac{\phi_c}{\phi_f} ; \frac{\phi_f}{\phi_c} \}$	$\mu_\phi^2(r_\phi^2) = \frac{1}{1 + \exp(-a_\phi^2(r_\phi^2 - c_\phi^2))}$

2) *Surface Length*: This rule aims at detecting the best candidate to represent the surface reflection by evaluating the length l_i of each candidate feature. Ideally, the length of the surface reflection is the same as the radargram in the azimuth direction. This can be evaluated with a sigmoid membership function (11) evaluating the attribute r_G . The attribute $r_G = l_i/l_R$ is defined as the ratio between the length l_i of each candidate feature and the radargram length l_R . In general, a sigmoid function is defined as follows:

$$\mu_j(r_j) = \frac{1}{1 + \exp(-a_j(r_j - c_j))} \quad (11)$$

where $\mu_j = \mu_G$ and $a_j = a_G$, $a_G > 0$ indicates the center of the function, and $c_j = c_G$, $c_G > 0$ is a parameter modeling the slope curvature. $\mu_G(r_G)$ returns a value in the range of $[0, 1]$; the higher the value of r_G , the higher the membership value and the possibility for that feature to be the candidate for the surface reflection. A low value of r_G indicates that the feature length is small compared to that of the radargram one. The best candidate to be the ground surface feature is identified with the aggregated membership value M_G , calculated by combining the completeness and surface length rules as in the following equation:

$$M_G = \mu_c \mu_G. \quad (12)$$

Among the fuzzy aggregation method, the Larsen product implication [40] is chosen since it is conservative. A small membership value forces a small final aggregation, regardless of the other membership values. The candidates are sorted considering their average depth. The feature with the lowest range coordinate, having an overall membership value M_G higher than a threshold Th_G , is classified as ω_g . The value M_G indicates the grade of reliability for that feature to be the best candidate to represent the surface reflection. Finally, the feature classified as ω_g is removed from \mathcal{F} to avoid the multiple labeling of the same feature.

The second step of the proposed method analyzes the remaining features $\mathcal{F} \setminus \{\mathbf{F}_i = \omega_g\}$ to detect possible candidates to represent the lava tube ceiling and floor. Ideally, the tube boundaries generate two reflections having a linear shape and comparable length. These reflections correspond to

the tube ceiling and floor, where the former is expected to have a lower range coordinate than the latter. Furthermore, the amplitude values of the two reflections are comparable since the void in the cavity only slightly attenuates the signal. Finally, the reflections are characterized by phase inversion due to the extreme difference between the dielectric materials at the interface. Hence, the related features need to match those in the EM model presented in Section II. The matching is evaluated by applying five fuzzy rules that analyze all the pairs of candidates. For each pair, the system provides a grade of membership that can be used to detect those representing tube boundaries. Couples of features are defined by choosing two features \mathbf{F}_c and \mathbf{F}_f in $\mathcal{F} = \{\mathbf{F}_i, i \in [1, \dots, N_F - 1]\}$ to be the candidate for the ceiling and the floor reflection, respectively. To identify the candidates, the features are sorted according to the increasing value of their average depth. Then, the candidates \mathbf{F}_c and \mathbf{F}_f are iteratively selected in a way that the average depth of \mathbf{F}_c is shallower than that of \mathbf{F}_f . At the i th iteration, the candidate are $\mathbf{F}_c = \mathbf{F}_i$ and $\mathbf{F}_f = \mathbf{F}_{i+1}$. If the candidates are evaluated by the fuzzy system to represent a possible lava tube, they are labeled $\mathbf{F}_c = \omega_c$ and $\mathbf{F}_f = \omega_f$ and both removed from \mathcal{F} . If this is not valid, the candidate feature for the floor is changed such that $\mathbf{F}_f = \mathbf{F}_{i+t}$, $t \in [1, \dots, N_F^i - 1]$, where N_F^i is the size of the feature set at the i th iteration. When $t = N_F^i$ and the candidate couples \mathbf{F}_c and \mathbf{F}_f are evaluated as not related lava tube boundaries, the candidate ceiling feature is set to $\mathbf{F}_c = \mathbf{F}_i = \omega_n$ and removed from \mathcal{F} . Then, at the next iteration $i + 1$, the candidate feature for the ceiling is changed and the above-mentioned procedure repeated. This approach stops when all the features in \mathcal{F} are labeled with one of the labels in $\Omega_c = \{\omega_g, \omega_c, \omega_f, \omega_n\}$. Each couple of candidate feature $\mathbf{F}_c = \{l_c, \rho_c, b_c, a_c, \phi_c\}$ and $\mathbf{F}_f = \{l_f, \rho_f, b_f, a_f, \phi_f\}$ is examined with the following rules that are summarized in Table III.

3) *Equivalence of Lengths*: This rule checks that the lengths of the candidate ceiling l_c and floor l_f features are similar. Ideally, when considering tubes with a cylindrical shape, the reflections generated by the boundaries of the tube have similar lengths. More realistically, reflections have a similar length rather than the same one. However, this is mitigated

by the fuzziness of the approach, and if needed, it can be considered explicitly in the definition of the rule by adding a margin on the similarity. This rule can be implemented with a sigmoid membership function (11) with $a_i = a_L$, $a_L > 0$ and $c_i = c_L$, $c_L > 0$ (see 11) that evaluates the attribute $r_L = \min\{l_c/l_f, l_f/l_c\}$. The function computes the membership value μ_L in the range of $[0, 1]$, which indicates the confidence to have similar lengths. μ_L is maximum when the candidates have a similar length. Decreasing the length of one feature decreases the value of μ_L .

4) *Proportionality*: This rule verifies that the candidate features overlap in the azimuth direction and thus eliminates a pair of features not sharing enough azimuth coordinates. Ideally, to represent a lava tube, the reflections should be completely overlapping in the azimuth direction. More realistically, reflections may not fully overlap. However, this is mitigated by the fuzziness of the approach. Also, for this rule, it can be included in the definition by including a margin. The proportionality membership μ_P is obtained by evaluating the attribute r_P with a sigmoid membership function (11) with $a_i = a_L$, $a_L > 0$ and $c_i = c_L$, $c_L > 0$. The attribute is $r_P = \min\{L/l_c, L/l_f\}$, where L is the number of pixels with the same azimuth coordinate in the candidate features. The higher the number of overlapping pixels, the higher is the membership value μ_P . μ_P goes to 0 when there are not overlapping pixels.

5) *Alignment of Barycenters*: This rule verifies that the candidate features are parallel. Ideally, approximating lava tubes as cylinders, the two reflections should be parallel to the azimuth direction. More realistically, the tube has a more complex shape, which, in radargrams, translates into reflections neither perfectly parallel to each other nor perfectly perpendicular to the range direction. Note that tubes can show a steepness coefficient higher than zero, i.e., the tube is inclined. Fixing $\alpha = 0$, the reflections in the radargram from the tube ceiling and floor may be neither parallel to the surface. Possible nonidealities of reflection barycenters not laying on the same line are mitigated by the fuzziness of the approach as the membership function gives a value indicating the goodness of the matching between the candidate features and the rule. To evaluate the alignment of the candidate features, the barycenter coordinates of the candidate features b_a^i and b_r^i in the azimuth and range directions, respectively, are considered as defined in Section III-B. According to the lava tube EM model, the barycenters of the two reflections lay on the same line, which is perpendicular to the azimuth direction. The slope m_{al} of the line connecting the barycenter of the two features is defined as

$$m_{al} = -\frac{b_r^c - b_r^f}{b_a^c - b_a^f}. \quad (13)$$

Finally, the slope of the line is compared with that of the azimuth direction. The attribute r_{al} considers the orientation of the range direction and the line passing in the barycenters of the tube reflections. Hence, the attribute is calculated as the angle between the two lines, i.e., $r_{al} = |m - m_{al}|$, where m is the orientation of the range direction. The membership function is a sigmoid membership function (11) with

parameters $a_i = a_{al}$, $a_{al} < 0$ and $c_i = c_{al}$, $c_{al} < 0$ since r_{al} is an angle in the range of $[-\pi/2, \pi/2]$. The value of r_{al} is 1 in the ideal case when the ceiling and floor features are parallel between them but perpendicular with the azimuth direction. r_{al} decreases to zero when the ceiling and floor features are not parallel between them nor perpendicular to the azimuth direction m .

6) *Amplitude Comparison*: This rule compares the amplitude signal of the candidate features among them and with that of the surface reflections. Ideally, the surface reflection has the highest amplitude in the radargram, and thus, the tube candidate features have a lower amplitude. The EM model indicates that the tube boundary reflections have a comparable amplitude signal since losses inside the tube are almost null. The difference in the amplitude signal is mitigated by the fuzziness of the approach. Attribute r_A is defined as $r_A = \min\{a_c/a_f, a_f/a_c\}$, where a_c and a_f are the mean amplitude of the candidate ceiling and floor candidate features, respectively. To compute μ_A , the attribute is evaluated with a sigmoid membership function (11) with $a_i = a_A$, $a_A > 0$ and $c_i = c_A$, $c_A > 0$. The membership value μ_A is maximum when the amplitude of the two reflections is similar, and it tends to zero when the difference is high.

7) *Phase Inversion*: This rule analyzes the phase of the candidate features. Ideally, a phase inversion occurs at each interface between materials with considerably different dielectric properties (see Section III-B). Here, two interfaces, i.e., the tube ceiling and bottom, generate the inversion of the phase signal. This rule is of critical importance to discriminate subsurface reflections of the tube boundaries from clutter. Clutter indicates the undesired reflections from the topography variations and the off-nadir surface due to the large antenna footprint. The surface clutter appears in the subsurface of the radargram when considering the acquisition time. The power of the clutter signal is higher than that of subsurface reflections. Since it may mask subsurface reflections, clutter can cause serious issues. However, the phase inversion is a property of subsurface echoes and helps in identifying clutter [36]. Here, the phase inversion is checked between: 1) the surface reflection and the candidate feature for the ceiling and 2) the candidate features for the tube ceiling and floor. The difference of the phase signals is calculated for the two cases according to (10). The phase difference considers the path traveled by the wave from one reflection to the other and the contribution from the dielectric interfaces. Here, the interest is in the contribution from the dielectric interfaces. Thus, the contribution given by the wave propagation is computed by considering the average depth of the reflection. The contribution given by the dielectric interfaces is computed by inverting (10). Ideally, the phase difference is equal to π , but more realistically, the phase difference may be slightly higher or lower. However, this is mitigated by the fuzziness of the proposed approach. The attributes for this rule r_ϕ^1 and r_ϕ^2 are computed by considering the phase contributions from the dielectric interfaces as follows:

$$r_\phi^1 = \min\{|\phi_c/\pi|; |\pi/\phi_c|\} \quad (14)$$

$$r_\phi^2 = \min\{|\phi_c/\phi_f|; |\phi_f/\phi_c|\} \quad (15)$$

where ϕ_c is the average relative phase of the candidate feature for the ceiling and ϕ_f is the average relative phase of the candidate feature for the floor. The attributes are evaluated with a sigmoid membership function (11) with $a_i = a_\phi$, $a_\phi > 0$ and $c_i = c_\phi$, $c_\phi > 0$ to have the membership values μ_ϕ^1 and μ_ϕ^2 . The memberships tend to 1 when the phase inversions occur for μ_ϕ^1 between the surface reflection and the candidate feature for the tube ceiling while for μ_ϕ^2 between the candidate features for the tube ceiling and floor.

For each couple of candidate features \mathbf{F}_c and \mathbf{F}_f , the membership values are aggregated with the Larsen product implication [40] as follows:

$$M_{cf} = \mu_C \mu_L \mu_P \mu_a^1 \mu_A \mu_\phi^1 \mu_\phi^2. \quad (16)$$

The value of the overall membership M_{cf} indicates the reliability for the candidate features \mathbf{F}_c and \mathbf{F}_f to represent the boundaries of a lava tube. The higher is M_{cf} , the higher is the probability that the candidate features are associated with lava tubes. The decision strategy consists of thresholding M_{cf} . When M_{cf} is larger than the empirically defined threshold Th_{tube} , the candidate reflections are associated with a candidate lava tube, such that $\mathbf{F}_c = \omega_c$ and $\mathbf{F}_f = \omega_f$. On the contrary, when $M_{cf} < Th_{\text{tube}}$, the candidate reflection is not associated with lava tubes reflection.

The parameters of the fuzzy memberships a_i and c_i in (11) indicate the grade of tolerance of the system. The sigmoid center c_i represents the case when the candidate features satisfy the rule with a membership of 0.5. The slope a_i indicates the flexibility of the system, i.e., the robustness of the rules to clutter, noise, and irregularity of the geometrical structures. Hence, c_i is fixed by considering the EM model for lava tubes. The slope a_i is empirically selected according to the data characteristics, e.g., the expected size of the cavities and the average interface depth in that area. The choice of c_i and a_i is related to the degree of fuzziness of the approach and, thus, to the grade of tolerance of the proposed method to the possible nonidealities of the candidate reflections. Considering the experimental results (see Section IV), one can conclude that the selection and tuning of the parameters are not critical and do not require complex prior knowledge.

IV. DESCRIPTION OF THE DATA SETS AND EXPERIMENTAL RESULTS

To assess the effectiveness of the proposed method, we carried out several experiments on two data sets. The first data set consists of data simulated with the approach proposed in [33] by: 1) varying the dimensions and depth of the tube according to [10] and [34] and 2) varying the characteristics of the terrain. The experiments on the simulated data set aim at proving the effectiveness and the validity of the proposed method in a controlled scenario. The second data set consists of radargrams acquired on the Moon by the LRS [38] onboard of the SELENE and ENgineering Explorer (SELENE) spacecraft. The results are validated by considering the state-of-the-art methods for detecting lava tubes, such as the superficial volcanic structures, the gravity and the thermal data, and eventual radar sounder measurements.

A. Simulated Data Set

The simulated data set consists of radargrams simulated with the setup described in Section II with the radar parameters in Table II. We performed two types of analyses by: 1) varying the geometry of the tubes and a smooth surface and 2) varying the surface topography and fixing the tube geometry. The first analysis aims to validate the proposed method in detecting lava tubes having different geometries, i.e., tube width and height, and roof thickness. The second analysis aims at understanding the impact of the topography of the surface, which generates clutter that masks the reflections of the subsurface on the performance of the proposed method.

1) *Description of the Data Set*: For the first analysis (geometry analysis), the geometries of the lava tube vary as in Table I, considering stable lava tube on the Moon according to [10] and [11]. The height of the tube is varied from 250 m up to 2 km, considering small, medium, and large lava tubes. The roof thickness varies accordingly, increasing up to 200 m, with the dimension of the tube. For all the geometries, we simulated different angles of intersection between the tube longitudinal axis and the moving direction of the radar (α): $\alpha = 0$ (parallel case) centered and off-centered, $\alpha = \pi/2$ (perpendicular case), and $\alpha \in (0, \pi/2)$ (diagonal cases). The difference between centered and off-centered simulations is in the axis where the lava tube is in the radargram, i.e., in the center of the tube or not. In the radargrams, this is reflected in the distance between the tube ceiling and floor reflections. The difference in the radargrams between the $\alpha = \pi/2$ and $\alpha \in (0, \pi/2)$ cases is in the length of the tube ceiling and floor (see Section II). For the analysis of the impact of the topography surface (terrain analysis), we fixed the tube dimension to 1000 m and the roof thickness to 75 m. We simulated three different surface topographies: smooth topography as a reference, surface with deep and large craters, and surface with deep and large craters and large roughness. Craters generate clutter reflections below the surface (see Fig. 2) which are not affected by the phase inversion. The surface roughness generates diffuse scattering around the reflection of the surface and the craters (see Fig. 2). For the terrain analysis, we performed simulation with $\alpha = 0$ (parallel case) and $\alpha = \pi/2$ (perpendicular case).

2) *Experimental Setup*: The first step is the extraction of the lines in the radargrams with the technique in [31]. The input parameters are estimated as in [31] and are reported in Table IV. The value of N_{AV} is set to 20 to guarantee an average probability of detection larger than 0.95 and a probability of false alarm of 10^{-3} . The value of Th_{line} is set to 60 by fixing the probability of false alarm to 10^{-3} after computing the conditional empirical noise distribution. The Viterbi length and excursion are experimentally set to 20 and 4, respectively. The Viterbi length indicates the maximum allowed range of the jump of the layer tracking from one azimuth position to another. Finally, the skeleton thickness is set to 10 pixels. It is worth noting that a relevant number of lines are extracted. Some are irrelevant from the application viewpoint as they are generated by the topography of the surface (clutter) or other subsurface structures. The topography increases the complexity of the problem of automatically

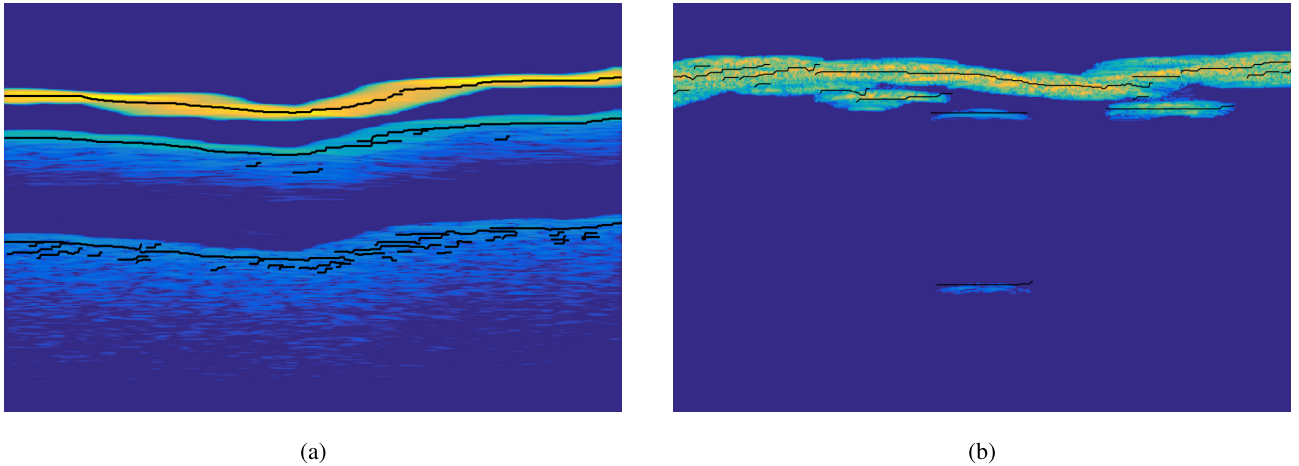


Fig. 7. Line detected (in black) with the technique in [31] for crossing angle values. (a) $\alpha = 0$. (b) $\alpha = \pi/2$. The case of a simulated radargram with a tube height of 1000 m and a roof thickness of 75 m and surface topography with a large roughness and thick craters is considered.

TABLE IV
VALUES OF THE PARAMETERS OF THE PROPOSED METHOD

Parameter	Simulated Dataset	LRS Dataset
N_{AV}	20	16
Viterbi length	20	20
Viterbi excursion	4	4
Th_{line}	40	40
Skeleton thickness	10 pixels	3 pixels
L_{min}	50 pixels	10 pixels
O_a	7 pixels	2 pixel
O_r	5 pixels	2 pixel
a_P, c_P	10, 0.3	10, 0.3
a_L, c_L	10, 0.5	10, 0.5
a_{al}, c_{al}	-10, $\frac{\pi}{3}$	-10, $\frac{\pi}{3}$
a_A, c_A	10, 0.5	10, 0.5
a_ϕ^1, c_ϕ^1	-10, 0.5	-10, 0.5
a_ϕ^2, c_ϕ^2	10, 0.5	10, 0.5
Th_G	0.50	0.50
Th_{tube}	0.1160	0.1160

detecting lava tube reflections. The second step of the proposed approach includes line refinement. The overlapping in azimuth and range is empirically set to $O_a = 7$ pixels and $O_r = 5$ pixels, respectively. Considering the azimuth resolution, the minimum feature length L_{min} is fixed to 50 pixels. The algorithm groups together segments that represent the same reflection as for the surface. Fig. 7 shows the outcome of the line detection algorithm for the simulations of a lava tube having an height of 1000 m and 75-m roof thickness with a surface characterized by a large roughness and thick craters with crossing angles $\alpha = 0$ [see Fig. 7(a)] and $\alpha = \pi/2$ [see Fig. 7(b)]. Figs. 8(a) and 9(a) show the outcome of the line refinement step with the extracted features in different colors. All the reflections are characterized by computing the length in pixels, the average depth and the barycenter coordinates in range and azimuth, and the average amplitude and phase values. For the phase evaluation, the Hanning window length T is estimated by considering the thickness of each reflection in the range direction. The relative dielectric properties of the rock are set to $\epsilon_r^{rock} = 4$ [41], whereas the relative dielectric

properties of the air are set to $\epsilon_r^{air} = 1$. The height of the radar above the surface is set to $h = 100$ km (see Table II). The third step analyzes the features with the fuzzy detection system to identify the best candidates to be the surface reflection and the lava tube ceiling and floor. For the detection of the surface reflection, the rule in (12) is evaluated with the parameters in Table IV. It is worth noting that the threshold Th_G was selected to minimize the missed alarms, considering the definition of the membership functions and the algebraic product as aggregation strategy (Larsen implication [40]). In this experiment, $\mu_G = 0.5$ and $\mu_p = 1$ were selected as a limit case, which results in an aggregate membership function for the surface of $M_G = \mu_G \mu_p = 0.5$, considering (12). Hence, $Th_G = 0.5$, as it is the value of M_G at the limit case. The aggregate membership value for the surface reflection was $M_G \geq 0.95$. The last step labels the reflection with ω_c and ω_f , and w_n . The parameters for the fuzzy rules memberships are in Table IV. $\mu_P = \mu_L = \mu_{al} = \mu_\phi = \mu_A = 0.7$ were selected as a limit cases, which result in an aggregate membership function for the tube detection of $M_{cf} = 0.1160$, considering (16). Hence, the lava tube threshold is set to $Th_{tube} = 0.1160$.

3) *Experimental Results:* The proposed method detected in all the radargrams the lava tubes with a high value of overall membership, i.e., higher than 0.98 in all the cases. It showed to detect lava tubes with different sizes, roof thickness, and crossing angle α , showing high robustness to the surface topography and the clutter in the simulated radargrams. For the sake of space, we report here only the analysis for two radargrams simulated with a tube height of 1000 m and a roof thickness of 75 m and surface topography characterized by large and deep craters and high roughness. Fig. 8 shows the processing for $\alpha = 0$ (parallel case); Fig. 8(a) shows the features extracted, whereas Fig. 8(a) shows the outcome of the detection algorithm (in blue the surface reflection and magenta the detected lava tube ceiling and floor). Fig. 9 shows the processing for $\alpha = \pi/2$ (perpendicular case). Note that the rule of the phase inversion is of major importance to discriminate between the clutter in the subsurface (generated by craters in the simulations) and the reflections from subsurface targets.

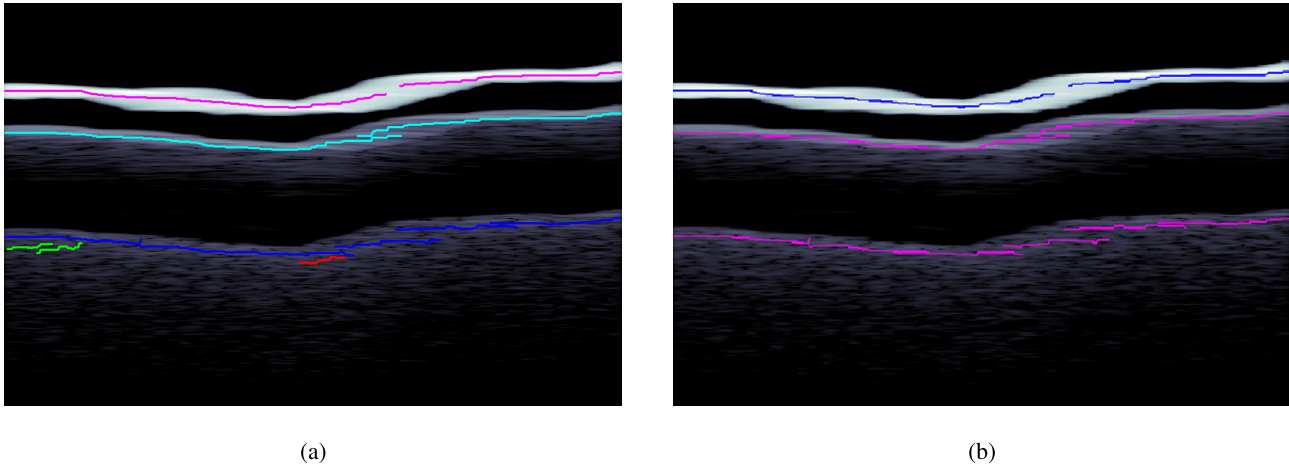


Fig. 8. Processing of the simulated radargram for $\alpha = 0$ (parallel case). (a) Extracted features in different colors. (b) Reflections recognized by the proposed approach as the surface in blue and the lava tube boundaries in magenta. The case of a tube having a height of 1000 m and a roof thickness of 75 m and surface topography with a large roughness and thick craters is considered.

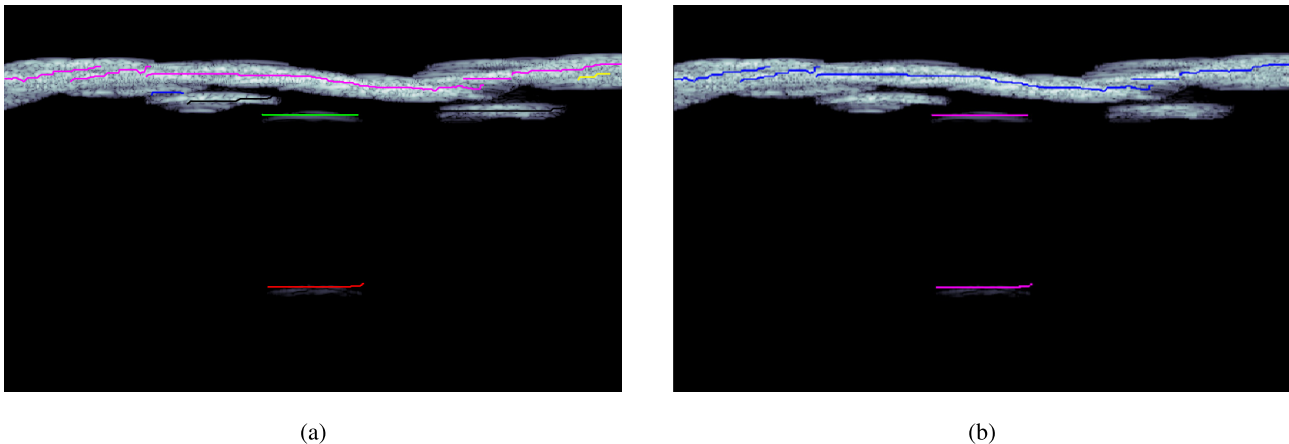


Fig. 9. Processing of the simulated radargram for $\alpha = \pi/2$. (a) Extracted features in different colors. (b) Reflections recognized by the proposed approach as the surface in blue and the lava tube boundaries in magenta. The case of a tube having a height of 1000 m and a roof thickness of 75 m and a surface topography with large roughness and thick craters is considered.

B. LRS Data Set

The second data set consists of radargrams acquired by the LRS onboard the SELENE spacecraft [38]. LRS had two dipoles of 30 m working at a frequency of 5 MHz. The characteristics allow penetration into the subsurface for some kilometers with a range resolution of 100 m in the vacuum. Table II summarizes the parameters of the LRS and the characteristics of the related radargrams. This section is structured as follows—first, we describe the data set in Section IV-B1, then, we analyze the radargram preprocessing and the experimental setup, and finally, we describe the experimental results in Section IV-B3.

1) *Description of the LRS Data Set:* The LRS data set considers radargrams acquired in: 1) the Marius Hills (MH) region, where lava tubes are expected in the subsurface due to the strong presence of superficial volcanic features and gravity evidence, and 2) in the highlands, where buried lava tubes are not expected, and the surface topography is affected by a large roughness and many impact craters [8], [42], [43]. In the MH region, the proposed method detects in an automatic and fast way candidate lava tubes in locations that are in line with the literature [8], [27], [42], [44], [45]. The reflections should be then further analyzed with a clutter simulator, but

we believe that this is out of the scope of this article. In the highlands, where lava tubes are not expected, we analyzed the rate of the false alarms, considering any reflection identified by the proposed method as a candidate lava tube as a false alarm. Hence, the number of false alarms N_{FA} is equal to the number of couples of reflections classified as candidate lava tubes.

a) *Marius hills:* MH (14° N, 56° W) is in the western equatorial region of Oceanus Procellarum. The region is a young pyroclastic deposit with a high concentration of volcanic features related to buried lava tubes, such as volcanic domes around 200–500 m high, rilles, pits, and depression lacking ejected rima. The characteristics of these geological formations are strongly different from others on the Moon [8], [42], [43], [46]. Hence, MH was an active volcanic region in recent years and with a high probability of having buried lava tubes. This is confirmed by the presence of C-shaped domes having a lower height and smaller diameter than others on the Moon. Another confirmation comes from the block abundance on the surface that makes the surface rougher than in the surrounding. The blocks have uniform size and are smaller than others in the surrounding, and thus, they are strongly different from the others on the Moon

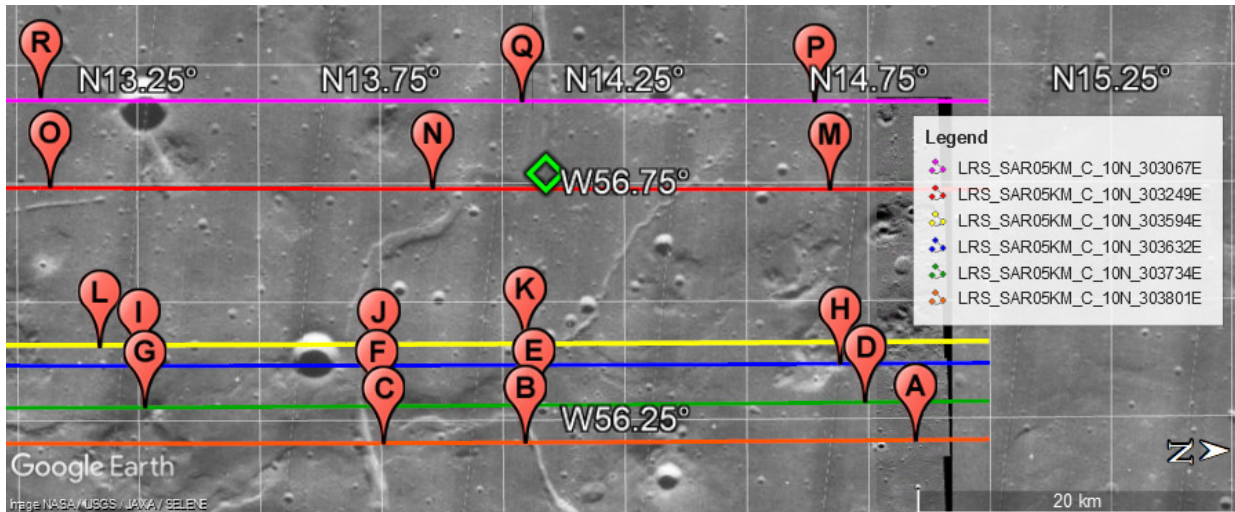


Fig. 10. MH region: lines are the tracks of the radargrams (see the legend for their ID). Candidate lava tube locations identified with the proposed method are indicated with the red pointers (optical image credits: NASA/GSFC/Arizona State University and NASA/USGS/JAXA/SELENE).

(such as those related to impact craters) [42]. The analysis of the pits in the MH region showed the presence of possible skylights, locally collapsed lava tube roof [8], [45]. Haruyama *et al.* [45] focused on the MH hole (see the green placemark in Fig. 10) that was imaged with oblique views by the LROC camera under different illuminations. The analysis of the images showed an extended subsurface void that can extend laterally in cavernous spaces. Hence, this hole is a candidate to be a skylight of a buried lava tube [45]. Furthermore, GRAIL data of the region show mass anomalies that can be explained with void volumes [47]. The size of the voids is comparable to that of empty and stable lava tubes, as defined in [10]. Finally, Kaku *et al.* [27] and Haruyama *et al.* [48] identified a possible location of lava tubes by analyzing rangelines of radargrams. Hence, the LRS data set for the MH region consists of six radargrams: LRS_SAR05KM_C_xxN_yyE with xxN_yyE in {10N_303594E, 10N_303632E, 10N_303067E, 10N_303734E, 10N_303249E, 10N_303801E}. Fig. 10 shows the radargram tracks in magenta superimposed on an optical image of the surface acquired by the Lunar Reconnaissance Orbiter Camera (LROC). The tracks are parallel to each other. Thus, it is reasonable to assume that a candidate lava tube in a radargram also appears in the other radargrams at a similar latitude.

b) Highlands: Highlands cover around 83% of the lunar surface and are characterized by impact craters. The surface topography is not flat, and thus, radargrams show a large number of clutter reflections in the subsurface. Lava tubes are not expected in these regions [8], [42], [43]. Hence, the LRS data set for the highlands region consists of hundred radargrams acquired in the rectangular area with latitude in the range of [45° N, 45° S] and longitude in the range of [90° E, 90° W].

2) *Experimental Setup:* Radargrams have n_T 1000 samples (rows), of which 500 are removed—200 from the radargram top as they represent the free space above the surface and 300 from the bottom as the signal-to-clutter ratio is low below ~ 3 km of penetration [27]. All radargrams have 8011 traces (columns). Radargrams of the MH are cut 807 traces to image

the latitude coordinates in the range of 13° N to 15° N, such as in [27] to focus on the MH region. All the radargrams are preprocessed with range compression to enhance the range resolution and SAR focusing [49] to enhance the azimuth resolution with a synthetic antenna length of 5 km.

As described in the methodological section (see Section III), the first step of the proposed approach is the extraction of the lines in the radargrams with [31]. The input parameters are estimated as in [31] and are reported in Table IV. For the LRS data set, the value of N_{AV} is set to 16 to guarantee an average probability of detection larger than 0.95 and a probability of false alarm of 10^{-3} for all the radargrams. The value of Th_{line} is set to 60 by fixing the probability of false alarm to 10^{-3} after computing the conditional empirical noise distribution. The Viterbi length and excursion are set to 20 and 4, respectively, for both the radargrams of the LRS data set. Finally, the skeleton thickness is set to 3 pixels. The second step of the proposed approach includes line refinement. The overlapping in azimuth and range is empirically set to $O_a = 2$ pixels and $O_r = 2$ pixels, respectively. Considering the LRS azimuth resolution, the minimum feature length L_{min} is fixed to 10 pixels. Hence, the smallest width of a possible lava tube is about 600 m, which should have a roof thickness of 50 m to be stable [10], [11]. In free space, the LRS range resolution is about 75 m, which is in the range of 100–150 m in the basaltic rock, which roughly corresponds to 1 pixel. The algorithm groups together segments that represent the same reflection, as for the surface. All the reflections are characterized by computing the length in pixels, the average depth and the barycenter coordinates in range and azimuth, and the average amplitude and phase values. For the phase evaluation, the length of the Hanning window T is estimated by considering the thickness of each reflection in the range direction. The relative dielectric properties of the rock are set to $\epsilon_r^{rock} = 4$ [41], whereas the relative dielectric properties of the air are set to $\epsilon_r^{air} = 1$. The height of the radar above the surface is set to $h = 100$ km (see Table II). The third step analyzes the features with the fuzzy detection system to identify the best candidate to be the surface reflection and the

TABLE V

OUTPUT VALUES OF THE PROPOSED METHOD FOR THE LRS DATA SET IN THE MH REGION: MEMBERSHIP VALUES FOR PAIRS OF REFLECTIONS IDENTIFIED CANDIDATE LAVA TUBES, COORDINATES OF THE LOCATIONS, AND TUBE HEIGHT AND ROOF THICKNESS ESTIMATED IN THE MID OF THE REFLECTIONS. IDS CORRESPOND TO THE LABELS IN Fig. 10

ID	μ_L	μ_s	μ_α	μ_P	μ_ϕ	M	Central Latitude	Central Longitude	Estimated Roof Thickness	Estimated Tube Height	Derived Tube Width
A	0.9086	0.9731	0.9733	0.9431	0.8999	0.7303	14.842 °N	303.798 °E	900 m	900 m	2.7 km
B	0.9861	0.9272	0.9963	0.9984	0.8979	0.8166	14.444 °N	303.798 °E	600 m	525 m	1575 m
C	0.9443	0.8489	0.9710	0.9620	0.9637	0.7216	13.723 °N	303.798 °E	700 m	600 m	1800 m
D	0.9768	0.9572	0.9536	0.9754	0.9436	0.8206	14.746°N	303.734°E	500 m	600 m	1.8 km
E	0.9286	0.9349	0.9982	0.9056	0.9168	0.7195	14.081°N	303.734°E	700 m	900 m	2.7 km
F	0.9774	0.9165	0.8968	0.9370	0.9509	0.7158	13.745°N	303.734°E	1 km	750 m	2250 m
G	0.9991	0.9645	0.9792	0.9179	0.9034	0.7825	13.253°N	303.734°E	800 m	675	2025 m
H	0.9825	0.9739	0.9907	0.9269	0.8997	0.7905	14.691°N	303.632°E	900 m	825 m	2475 m
I	0.9286	0.9349	0.9982	0.9056	0.8368	0.6567	14.253°N	303.632°E	800 m	1125 m	3375 m
J	0.9830	0.9753	0.9801	0.9538	0.9418	0.8441	13.824°N	303.632°E	700 m	525 m	1575 m
K	0.9706	0.9330	0.9082	0.9276	0.8957	0.6833	14.016°N	303.594°E	1.3 km	1050 m	3150 m
L	0.9924	0.9355	0.9544	0.9706	0.9361	0.8051	13.173°N	303.594°E	1.2 km	975 m	2925 m
M	0.9954	0.9882	0.9367	0.9343	0.8806	0.7581	14.672°N	303.594°E	1.1 km	600 m	1.8 km
N	0.9369	0.9628	0.9887	0.9701	0.9331	0.8073	13.864°N	303.262°E	500 m	675 m	2025 m
O	0.9815	0.9679	0.9413	0.9726	0.8684	0.7553	13.052°N	303.594°E	1 km	750 m	2250 m
P	0.9589	0.9964	0.9670	0.8863	0.8925	0.7308	14.643°N	303.264°E	1.4 km	1050 m	3150 m
Q	0.9286	0.9349	0.9982	0.9541	0.9087	0.7513	13.861°N	303.263°E	1.3 km	975 m	2925 m
R	0.9951	0.8927	0.9524	0.9374	0.8798	0.6978	13.051°N	303.262°E	1.1 km	450 m	1350 m

best candidates to be reflections generated by the lava tube ceiling and floor. For the detection of the surface reflection, rule in (12) is evaluated with the parameters in Table IV. It is worth noting that the threshold T_G was selected to minimize the missed alarms, considering the definition of the membership functions and the algebraic product as aggregation strategy (Larsen implication [40]). In this experiment, $\mu_G = 0.5$ and $\mu_p = 1$ were selected as limit cases, which results in an aggregate membership function for the surface of $M_G = \mu_G \mu_p = 0.5$, considering (12). Hence, $\text{Th}_G = 0.5$, as the value of M_G at the limit case. The aggregate membership value for the surface reflection was $M_G \geq 0.71$. The last step labels the reflection with ω_c and ω_f , and w_n . The parameters for the fuzzy rules memberships are in Table IV. $\mu_P = \mu_L = \mu_{al} = \mu_\phi = \mu_A = 0.7$ were selected as limit cases, which result in an aggregate membership function for the tube detection of $M_{cf} = 0.1160$, considering (16). Hence, the lava tube threshold is set to $\text{Th}_{\text{tube}} = 0.1160$.

3) *Experimental Results*: This section describes the experimental results for radargrams acquired in the MH and highlands.

a) *Marius hills*: The method identified 20 candidate lava tubes in the LRS data set—in Fig. 10, the detected tubes are in red. Table V lists the fuzzy rule membership values and the tunnels estimated parameters. Note that the aggregate membership values are all above 0.65. M_G and M_{cf} can be considered as a grade of reliability that the couples of reflections are related to a buried candidate lava tube. For the sake of space, Fig. 11 shows the steps of the proposed method for the candidate tube C. Identified candidate lava tubes correspond with those in [27]. Reflections of the identified candidate lava tubes should be further analyzed with a clutter

simulator to discriminate subsurface reflections from clutter (this is outside the scope of this article).

Assuming that the reflections are generated by lava tubes, we can estimate the roof thickness and the tube dimension. The roof thickness is estimated by considering the depth of the ceiling reflection to the surface and $\epsilon_r^{\text{rock}} = 4$ as the rock relative dielectric constant [41]. The tube height is estimated by considering: 1) the difference between the depth of the tube ceiling and the floor and 2) a void tube $\epsilon_r^{\text{void}} = 1$. The tube width cannot be correctly estimated as it depends on the length of the reflection and the crossing angle between the moving direction of the radar and the longitudinal axis of the tube, which is unknown. The estimations in Table V are computed by considering that: 1) the moving direction of the radar is perpendicular to the longitudinal axis of the tube and 2) the ratio between the tube height and width is 1:3 as in [10]. Hence, the tube width is calculated by multiplying the tube height by 3 to understand whether it may exist such a stable tube on the Moon according to [10]. Considering their height and roof thickness, tunnels identified by the proposed method can exist and can be stable on the Moon (i.e., not collapsed) under the Lithostatic and the Poisson stress states.

b) *Highlands*: The method identifies $N_{\text{LT}} = 12$ couple of reflections of candidate lava tubes. The average overall membership value is equal to 0.3205, which is much lower than the minimum overall membership value of the candidate lava tubes detected in the MH region. Since in the highlands lava tubes are not expected, the number of false alarms is set equal to $N_{\text{FA}} = 12$. The false alarm rate ζ_{FA} is defined as

$$\zeta_{\text{FA}} = \frac{N_{\text{FA}}^a}{N_{\text{TOT}}^a} \quad (17)$$

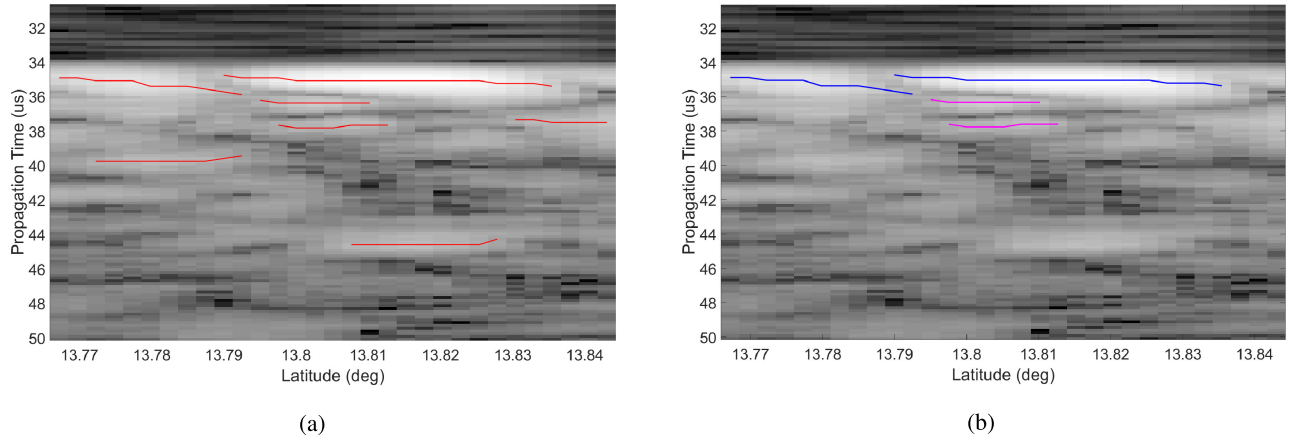


Fig. 11. Analysis of the part of the radargram LRS_SAR05KM_C_10N_303801E between 13.75° N and 13.85° N. (a) Extracted features. (b) Reflections indicated by the proposed approach as the surface in blue and the candidate lava tube boundaries in magenta. The placemark of this tube is C in Fig. 10.

where N_{FA}^a indicates the number of rangelines (traces) covered by the candidate lava tubes (false alarms) and N_{TOT}^a indicates the total number of traces being processed. The total number of traces is equal to $N_{TOT}^a = 801\,100$ since each radargram has 8011 traces and we analyzed 100 radargrams. The number of false alarm rangelines N_{FA}^a is defined as the sum of the length in the azimuth of candidate lava tubes. For each detected lava tube candidate i , we considered the length of the longer features, i.e., $l^i = \max\{l_c^i, l_f^i\}$. Hence, the number of false alarm rangelines is defined as $N_{FA}^a = \sum l_i, i = [1, \dots, N_{LT}]$. For the LRS radargrams in the highlands, $N_{FA}^a = 127$, and thus, the false alarm rate is $\zeta_{FA} = 1.5853 \times 10^{-4}$. Note that the false alarm rate is estimated for the LRS radargrams considered in the Highland area, and it may vary by region and data sets.

V. DISCUSSION

The core assumption of the proposed method is the detection of the reflections from the tube ceiling and floor and the surface. This assumption is not always valid as it depends on the acquisition system and the dimension of the target. The proposed EM model of lava tubes assumes that the range resolution of the radargram is high enough to image the surface and the tube ceiling and floor. Under this assumption, the proposed method is demonstrated to be effective. However, stable and empty lava tubes exist on the Moon and Mars with a thin roof [10], [34] smaller than the range resolution of the radar sounder. Therefore, in radar sounder data, the lava tube ceiling may be masked and incorporated in the surface reflection and, thus, not detectable.

Another assumption of the proposed method is that the signal-to-noise ratio (SNR) is high enough to detect the reflections of the tube ceiling and floor. Relevant factors in the SNR are the attenuation of the subsurface, the depth of the floor reflection, and the two-way rough surface transmission loss (depending on the frequency). The SNR also impacts the error of the phase signal. Considering the properties of the Maria on the Moon, the study in [36] showed that an SNR > 10 dB is enough to detect lava tubes and to guarantee a negligible absolute phase error. Further information about the SNR analysis can be found in [36], where the SNR estimation

and impact on the absolute error phase are described in detail. Radargrams with low SNR values show dense and fragmented reflections, i.e., subsurface targets are imaged with discontinuous reflections. The considered line detection algorithm is suitable to process radargrams with low SNR as the HMM and the VA are applied with a divide-and-conquer strategy [31]. The line refinement step groups together lines belonging to the same reflection.

The proposed method analyzes radargram reflections as candidates to be the lava tube ceiling or floor. Identified candidate lava tubes should be then studied in postprocessing by expert planetologists to detect possible unidentified clutter reflections and make the final decision. However, it is worth noting that surface clutter does not generate any phase inversion [36], and thus, Rule 7 (phase inversion rule) is likely to assume a small value, bringing to a small overall membership. An example of a geological structure that generates reflections with a geometry similar to that of lava tubes is craters (see Fig. 2). Crater reflections do not generate phase inversion—Rule 7 has a small membership value, which leads to an overall small membership value.

VI. CONCLUSION

This article proposed a novel method to detect candidate buried cavities, such as empty lava tubes, in radar sounder data. The approach consists of three main steps: 1) EM and geometric modeling of the lava tube by considering the propagation of the EM wave in the subsurface; 2) extraction and characterization of relevant reflections in a radargram; and 3) analysis of the reflections to identify those related to the surface and lava tube ceiling and floor and associate them with a grade of reliability.

The method takes advantage of the theoretical modeling of how cavities and lava tubes appear in radargrams. The model describes the physical properties of the reflection generated by the surface and subsurface cavities. From this model, the surface and lava tube boundaries can be identified by a pattern of linear reflections with specific alignment, geometrical, and signal properties. The candidate linear reflections are analyzed with a fuzzy system based on the lava tube model. The fuzzy rules consider the backscattering mechanisms of

buried and empty lava tubes imaged by radar sounders and provide a membership value that indicates the reliability of each detected tunnel. The proposed approach requires the tuning of some parameters that depend on the approximated size of the expected lava tubes in the investigated area and the radar range and azimuth resolutions. This information is usually available and easy to include in the processing. After tuning, the method is automatic and unsupervised.

The effectiveness of the proposed method has been demonstrated with experiments on two data sets: simulated and real LRS data sets. The accurate detection of the lava tubes in the simulated data set demonstrated that the method is effective and accurate in detecting lava tubes in radargrams with: 1) different dimension and depth values; 2) different crossing angles between the tube axis and moving direction of the spacecraft; and 3) varying surface topography. The results showed the high robustness of the proposed method to deviations from the ideal lava tube model due to the definition of adequate fuzzy rules. For the LRS data set, the proposed method analyzed radargrams in the Maria region (MH) where lava tubes are expected and in the highlands area where lava tubes are not expected. In the MH region, the proposed method identified in a completely automatic way several candidate lava tubes that were already documented in the literature. This resulted in a fast detection that would not be possible in a large number of radargrams with state-of-the-art methods based on the visual inspection of surficial volcanic features. Identified candidate lava tubes should be further analyzed with a clutter simulator to make a reliable final decision on them. It is worth noticing that the comparison of the identified reflections with the clutter simulations requires a dedicated analysis that goes beyond the scope of this article. In the highlands regions, we analyzed 100 radargrams characterized by the presence of a large amount of surface clutter due to the irregularities of the surface topography. The proposed method resulted in a false alarm rate of $\zeta_{FA} = 1.5853 \times 10^{-4}$. Note that the false alarm rate is an estimate for the data set considered in the Highlands areas, and it may vary by region and data sets. The low false alarm rate is mainly due to the phase inversion rule, in which the membership assumes small values with clutter (as there is no phase inversion), bringing to a small overall membership. Hence, the phase inversion rule showed to increase the robustness of the proposed method against the clutter.

As future development, we plan to improve the EM model of lava tube to consider cavities totally or half-filled with other materials, such as regolith and rock. We also intend to further analyze the detected candidate lava tube reflections on the MH and the Moon by comparing them to clutter simulations. Finally, we plan to model other targets of planetary arid areas, such as craters and tesserae, and design rules to include them in the system.

ACKNOWLEDGMENT

The authors would like to thank the anonymous reviewers for the helpful comments and suggestions that contribute to improve this article. They would also like to

thank the SELENE (KAGUYA) LRS team and the SELENE Data Archive for providing the SELENE (KAGUYA) data. SELENE is a Japanese mission developed and operated by JAXA.

REFERENCES

- [1] H. Miyamoto *et al.*, "Mapping the structure and depth of lava tubes using ground penetrating radar," *Geophys. Res. Lett.*, vol. 32, no. 21, 2005, Art. no. L21316.
- [2] A. S. Arya, P. R. Rudravaram, G. Thangjam, A. Prof, and K. K. Seelin, "Detection of potential site for future human habitability on the Moon using Chandrayaan-1 data," *Current Sci.*, vol. 100, pp. 524–529, Feb. 2011.
- [3] G. Hulme, "The interpretation of lava flow morphology," *Geophys. J. Int.*, vol. 39, no. 2, pp. 361–383, Nov. 1974.
- [4] S. E. Braden, J. D. Stopar, M. S. Robinson, S. J. Lawrence, C. H. van der Bogert, and H. Hiesinger, "Evidence for basaltic volcanism on the Moon within the past 100 million years," *Nature Geosci.*, vol. 7, no. 11, pp. 787–791, Nov. 2014.
- [5] S. J. Robbins, G. D. Achille, and B. M. Hynek, "The volcanic history of Mars: High-resolution crater-based studies of the calderas of 20 volcanoes," *Icarus*, vol. 211, no. 2, pp. 1179–1203, Feb. 2011.
- [6] J. J. Papike, G. Ryder, and C. K. Shearer, "Lunar samples," *Rev. Mineral. Geochem.*, vol. 36, no. 1, pp. 5.1–5.234, Jan. 1998.
- [7] S. Kempe and M. S. Werner, "The Kuka'iau Cave, Mauna Kea, Hawaii, created by water erosion: A new Hawaiian cave type," *J. Cave Karst Stud.*, vol. 65, no. 1, pp. 53–67, 2003.
- [8] F. Sauro, R. Pozzobon, M. Massironi, P. De Berardinis, T. Santagata, and J. De Waele, "Lava tubes on Earth, Moon and Mars: A review on their size and morphology revealed by comparative planetology," *Earth-Sci. Rev.*, vol. 209, Oct. 2020, Art. no. 103288.
- [9] C. R. Rowell, A. Pidlisecky, J. D. Irving, and R. J. Ferguson, "Characterization of lava tubes using ground penetrating radar at craters of the Moon national monument, USA," *Crewes, Univ. Calgary, Calgary, AB, Canada, CREWES Res. Rep.* 22, 2017, pp. 1–18, vol. 22.
- [10] D. M. Blair *et al.*, "The structural stability of lunar lava tubes," *Icarus*, vol. 282, pp. 47–55, Jan. 2017.
- [11] A. E. Theinat *et al.*, "Geometry and structural stability of lunar lava tubes," in *Proc. AIAA SPACE Astronaut. Forum Expo.* Reston, VA, USA: American Institute of Aeronautics and Astronautics, Sep. 2018, p. 5185.
- [12] H. Benaroya, "Lunar habitats: A brief overview of issues and concepts," *Reach*, vols. 7–8, pp. 14–33, Dec. 2017.
- [13] G. Cushing, "Candidate cave entrances on mars," *J. Cave Karst Stud.*, vol. 74, no. 1, pp. 33–47, Apr. 2012.
- [14] G. E. Cushing, C. H. Okubo, and T. N. Titus, "Atypical pit craters on Mars: New insights from THEMIS, CTX, and HiRISE observations," *J. Geophys. Res., Planets*, vol. 120, no. 6, pp. 1023–1043, Jun. 2015.
- [15] F. Horz, "Lava tubes-potential shelters for habitats," in *Lunar Bases Space Activities 21st Century*. Houston, TX, USA: Lunar and Planetary Institute, 1985, pp. 405–412.
- [16] P. J. Boston, "Extraterrestrial subsurface technology test bed: Human use and scientific value of martian caves," *AIP Conf.*, vol. 699, pp. 1007–1018, Feb. 2004.
- [17] D. Rapp, "Radiation effects and shielding requirements in human missions to the Moon and Mars," *Mars J.*, vol. 2, pp. 46–71, Sep. 2006.
- [18] R. J. Léveillé and S. Datta, "Lava tubes and basaltic caves as astrobiological targets on Earth and Mars: A review," *Planet. Space Sci.*, vol. 58, no. 4, pp. 592–598, Mar. 2010.
- [19] A. Z. Miller *et al.*, "Exploring possible Mars-like microbial life in a lava tube from Lanzarote: Preliminary results of *in-situ* DNA-based analysis as part of the PANGAEA-X test campaign," in *Proc. EGU Gen. Assem. Conf. Abstr. (EGUGA)*, Apr. 2018, p. 1258.
- [20] D. P. Cruikshank and C. A. Wood, "Lunar rilles and Hawaiian volcanic features: Possible analogues," *Moon*, vol. 3, no. 4, pp. 412–447, Mar. 1972.
- [21] A. G. Taylor and A. Gibbs, "Automated search for lunar lava tubes in the clementine dataset," in *Proc. New Views Moon, Integr. Remotely Sensed, Geophys., Sample Datasets*, 1998, p. 70.
- [22] S. J. Lawrence *et al.*, "LRO observations of morphology and surface roughness of volcanic cones and lobate lava flows in the Marius hills," *J. Geophys. Res., Planets*, vol. 118, no. 4, pp. 615–634, Apr. 2013.
- [23] R. V. Wagner and M. S. Robinson, "Distribution, formation mechanisms, and significance of lunar pits," *Icarus*, vol. 237, pp. 52–60, Jul. 2014.
- [24] D. Wyrick, "Distribution, morphology, and origins of martian pit crater chains," *J. Geophys. Res.*, vol. 109, no. E6, pp. 1–20, 2004.

- [25] G. E. Cushing, T. N. Titus, J. J. Wynne, and P. R. Christensen, "THEMIS observes possible cave skylights on Mars," *Geophys. Res. Lett.*, vol. 34, no. 17, 2007, Art. no. L17201.
- [26] L. Chappaz *et al.*, "Evidence of large empty lava tubes on the Moon using GRAIL gravity," *Geophys. Res. Lett.*, vol. 44, no. 1, pp. 105–112, Jan. 2017.
- [27] T. Kaku *et al.*, "Detection of intact lava tubes at Marius hills on the Moon by SELENE (Kaguya) lunar radar sounder," *Geophys. Res. Lett.*, vol. 44, no. 20, pp. 10–155, Oct. 2017.
- [28] T. Kobayashi, J.-H. Kim, S. R. Lee, and K.-Y. Song, "Nadir detection of lunar lava tube by Kaguya lunar radar sounder," *IEEE Trans. Geosci. Remote Sens.*, early access, Nov. 11, 2020, doi: [10.1109/TGRS.2020.3033033](https://doi.org/10.1109/TGRS.2020.3033033).
- [29] E. Donini, S. Thakur, F. Bovolo, and L. Bruzzone, "An automatic approach to map refreezing ice in radar sounder data," *Proc. SPIE*, vol. 11155, Oct. 2019, Art. no. 111551B.
- [30] E. Donini, F. Bovolo, C. Gerekos, L. Carrer, and L. Bruzzone, "An approach to lava tube detection in radar sounder data of the Moon," in *Proc. Int. Geosci. Remote Sens. Symp. (IGARSS)*, Jul. 2018, pp. 8424–8427.
- [31] L. Carrer and L. Bruzzone, "Automatic enhancement and detection of layering in radar sounder data based on a local scale hidden Markov model and the Viterbi algorithm," *IEEE Trans. Geosci. Remote Sens.*, vol. 55, no. 2, pp. 962–977, Feb. 2017.
- [32] A. Ferro and L. Bruzzone, "Automatic extraction and analysis of ice layering in radar sounder data," *IEEE Trans. Geosci. Remote Sens.*, vol. 51, no. 3, pp. 1622–1634, Mar. 2013.
- [33] C. Gerekos, A. Tamponi, L. Carrer, D. Castelletti, M. Santoni, and L. Bruzzone, "A coherent multilayer simulator of radargrams acquired by radar sounder instruments," *IEEE Trans. Geosci. Remote Sens.*, vol. 56, no. 12, pp. 7388–7404, Dec. 2018.
- [34] A. K. Theinat *et al.*, "Lunar lava tubes: Morphology to structural stability," *Icarus*, vol. 338, Mar. 2020, Art. no. 113442.
- [35] D. W. Strangway and G. R. Olhoeft, "Electrical properties of planetary surfaces," *Phil. Trans. Roy. Soc. London A, Math. Phys. Sci.*, vol. 285, no. 1327, pp. 441–450, 1977.
- [36] L. Carrer, C. Gerekos, and L. Bruzzone, "A multi-frequency radar sounder for lava tubes detection on the Moon: Design, performance assessment and simulations," *Planet. Space Sci.*, vol. 152, pp. 1–17, Mar. 2018.
- [37] F. J. Harris, "On the use of windows for harmonic analysis with the discrete Fourier transform," *Proc. IEEE*, vol. 66, no. 1, pp. 51–83, Jan. 1978.
- [38] T. Ono *et al.*, "Lunar radar sounder (LRS) onboard the KAGUYA (SELENE) spacecraft," *Space Sci. Rev.*, vol. 154, nos. 1–4, pp. 145–192, Jul. 2010.
- [39] S. Esmacili *et al.*, "Resolution of lava tubes with ground penetrating radar: The TubeX project," *J. Geophys. Res., Planets*, vol. 125, no. 5, May 2020, Art. no. e2019JE006138.
- [40] P. M. Larsen, "Industrial applications of fuzzy logic control," *Int. J. Man-Mach. Stud.*, vol. 12, no. 1, pp. 3–10, 1980.
- [41] D. H. Chung, W. B. Westphal, and G. Simmons, "Dielectric properties of Apollo 11 lunar samples and their comparison with Earth materials," *J. Geophys. Res.*, vol. 75, no. 32, pp. 6524–6531, Nov. 1970.
- [42] S. J. Lawrence *et al.*, "LRO observations of morphology and surface roughness of volcanic cones and lobate lava flows in the Marius Hills," *J. Geophys. Res., Planets*, vol. 118, no. 4, pp. 615–634, 2013.
- [43] R. Greeley, "Lava tubes and channels in the lunar Marius hills," *Moon*, vol. 3, no. 3, pp. 289–314, Dec. 1971.
- [44] R. Sood, L. Chappaz, H. Melosh, K. Howell, and C. Milbury, "Detection of buried empty lunar lava tubes using grail gravity data," in *Proc. Lunar Planet. Sci. Conf.*, 2016, p. 1509.
- [45] J. Haruyama *et al.*, "Possible lunar lava tube skylight observed by SELENE cameras," *Geophys. Res. Lett.*, vol. 36, no. 21, 2009, Art. no. L21206.
- [46] B. E. Walden, T. L. Billings, C. L. York, S. L. Gillett, and M. V. Herbert, "Utility of lava tubes on other worlds," in *Proc. Using Situ Resour. Construct. Planet. Outposts*, 1998, p. 16.
- [47] W. S. Kiefer, "Gravity constraints on the subsurface structure of the Marius hills: The magmatic plumbing of the largest lunar volcanic dome complex," *J. Geophys. Res., Planets*, vol. 118, no. 4, pp. 733–745, Apr. 2013.
- [48] J. Haruyama *et al.*, "Detection of lunar lava tubes by lunar radar sounder onboard selene (Kaguya)," in *Proc. Lunar Planet. Sci. Conf.*, 2017, p. 1711.

- [49] T. Kobayashi *et al.*, "Synthetic aperture radar processing of Kaguya lunar radar sounder data for lunar subsurface imaging," *IEEE Trans. Geosci. Remote Sens.*, vol. 50, no. 6, pp. 2161–2174, Jun. 2012.



Elena Donini (Graduate Student Member, IEEE) received the B.Sc. degree in electronics and telecommunication engineering and the M.Sc. degree (*summa cum laude*) in telecommunication engineering from the University of Trento, Trento, Italy, in 2015 and 2017, respectively. She is pursuing the Ph.D. degree with Remote Sensing Laboratory, Department of Information and Communication Technologies, University of Trento, and the Remote Sensing for Digital Earth Unit, Fondazione Bruno Kessler, Trento.

She is a member of the scientific team working on the Radar for Icy Moon Exploration (RIME) Instrument, which will be onboard the upcoming ESA mission JUPITER ICy moons Explorer (JUICE) to the Jupiter system. Her research interests are related to the automatic analysis of radar sounder data with machine learning and deep learning.

Ms. Donini was a recipient of the prize for the 2017 Best Italian master Thesis in remote sensing awarded by the Italy Chapter of the IEEE Geoscience and Remote Sensing Society.



Leonardo Carrer (Member, IEEE) received the M.Sc. degree (Hons.) in electrical engineering from the Delft University of Technology, Delft, The Netherlands, in 2012, and the Ph.D. degree in communication and information technology from the University of Trento, Trento, Italy, in 2018.

In 2017, he was a Visiting Researcher at Stanford University, Stanford, CA, USA, working on passive radio sounding of icy moons using nonwhite Jovian noise. He is an Assistant Professor (RTD-A) with the University of Trento. He is a member of the scientific team working on the Radar for Icy Moon Exploration (RIME) instrument, which will be onboard the upcoming ESA mission JUPITER ICy moons Explorer (JUICE) to the Jupiter system. He publishes on peer-reviewed journals both in the remote sensing and planetary and space research communities. His research interests include radar sounders system engineering, performance models, and advanced signal processing.

Dr. Carrer was a recipient of the Best Student Paper Award of the SPIE Remote Sensing Conference with a work on bio-inspired radar sounding in 2016 and the IEEE-GRS29-CNI Best PhD Thesis Award 2018 for the best three Ph.D. thesis in the area of geoscience and remote sensing (GRS) in 2018.



Christopher Gerekos received the bachelor's and master's degrees (Hons.) in physics from the Université Libre de Bruxelles, Brussels, Belgium, in 2013 and 2016, respectively, and the Ph.D. degree (Hons.) in telecommunications engineering from the Università degli Studi di Trento, Trento, Italy, in 2020.

In 2015, while at the Advanced Concepts Team of the European Space Agency (ESA), Noordwijk, The Netherlands, he worked on relativistic positioning systems, a class of descriptions of global navigation satellite systems that rely purely on the general theory of relativity. From 2016 to 2020, he was part of the team working on the Radar for Icy Moon Exploration (RIME) Instrument of the Jupiter Icy moons Explorer (JUICE) Mission of ESA. He conceived an efficient coherent radar echo simulator specifically tailored to planetary radar sounding. In 2019, he was a Visiting Ph.D. Student at The University of Texas at Austin, Austin, TX, USA, where he worked on high-precision altimetry with radar sounders and on studying the fractal properties of the Jovian moon Europa and he was also part of the Science Data System of Europa Clipper's REASON (Radar for Europa Assessment and Sounding: Ocean to Near-surface) Instrument, in charge of elaborating and maintaining the algorithms relevant to the science of REASON. His research interests include computational electromagnetics and radar sounder design.



Lorenzo Bruzzone (Fellow, IEEE) received the Laurea (M.S.) degree (*summa cum laude*) in electronic engineering and the Ph.D. degree in telecommunications from the University of Genoa, Genoa, Italy, in 1993 and 1998, respectively.

He is a Full Professor of telecommunications with the University of Trento, Trento, Italy, where he teaches remote sensing, radar, and digital communications. He is the Founder and the Director of Remote Sensing Laboratory, Department of Information Engineering and Computer Science, University of Trento. His research interests are in the areas of remote sensing, radar and synthetic aperture radar (SAR), signal processing, machine learning, and pattern recognition. He promotes and supervises research on these topics within the frameworks of many national and international projects. He is the Principal Investigator of many research projects. Among the others, he is the Principal Investigator of the Radar for icy Moon Exploration (RIME) Instrument in the framework of the JUPITER ICy moons Explorer (JUICE) Mission of the European Space Agency (ESA) and the Science Lead for the High-Resolution Land Cover project in the framework of the Climate Change Initiative of ESA. He is the author (or coauthor) of 294 scientific publications in refereed international journals (221 in IEEE journals), more than 340 papers in conference proceedings, and 22 book chapters. He is the editor/the coeditor of 18 books/conference proceedings and one scientific book. His papers are highly cited, as proven from the total number of citations (more than 37 000) and the value of the H-index (89) (source: Google Scholar).

Dr. Bruzzone ranked first place in the Student Prize Paper Competition of the 1998 IEEE International Geoscience and Remote Sensing Symposium (IGARSS), Seattle, in July 1998. He was a recipient of many international and national honors and awards, including the recent IEEE GRSS 2015 Outstanding Service Award, the 2017 and 2018 IEEE IGARSS Symposium Prize Paper Awards, and the 2019 WHISPER Outstanding Paper Award. He was a Guest Coeditor of many special issues of international journals. He is the Co-Founder of the IEEE International Workshop on the Analysis of Multi-Temporal Remote-Sensing Images (MultiTemp) series and is a member of the Permanent Steering Committee of this series of workshops. He was invited as a keynote speaker in more than 40 international conferences and workshops. Since 2003, he has been the Chair of the SPIE Conference on Image and Signal Processing for Remote Sensing. Since 2009, he has been a member of the Administrative Committee of the IEEE Geoscience and Remote Sensing Society (GRSS), where he has been the Vice-President for Professional Activities since 2019. He has been the Founder of the *IEEE Geoscience and Remote Sensing Magazine*, for which he has been the Editor-in-Chief from 2013 to 2017. He is an Associate Editor for the IEEE TRANSACTIONS ON GEOSCIENCE AND REMOTE SENSING. He has been a Distinguished Speaker of the IEEE Geoscience and Remote Sensing Society from 2012 to 2016.



Francesca Bovolo (Senior Member, IEEE) received the Laurea (B.S.) degree, the Laurea Specialistica (M.S.) degree (*summa cum laude*) in telecommunication engineering, and the Ph.D. degree in communication and information technologies from the University of Trento, Trento, Italy, in 2001, 2003, and 2006, respectively.

She was a Research Fellow with the University of Trento until 2013. She is the Founder and the Head of the Remote Sensing for Digital Earth Unit, Fondazione Bruno Kessler, Trento, and a member of Remote Sensing Laboratory. She is one of the co-investigators of the Radar for Icy Moon Exploration Instrument of the European Space Agency Jupiter Icy Moons Explorer and a member of the science study team of the EnVision mission to Venus. Her research interests include remote-sensing image processing, multitemporal remote sensing image analysis, change detection in multispectral, hyperspectral, and synthetic aperture radar images, and very high-resolution images, time series analysis, content-based time series retrieval, domain adaptation, and Light Detection and Ranging (LiDAR) and radar sounders. She conducts research on these topics within the context of several national and international projects.

Dr. Bovolo is a member of the program and scientific committee of several international conferences and workshops. She was a recipient of the First Place in the Student Prize Paper Competition of the 2006 IEEE International Geoscience and Remote Sensing Symposium, Denver, in 2006. She was the Technical Chair of the Sixth International Workshop on the Analysis of Multitemporal Remote-Sensing Images (MultiTemp 2011 and 2019). She has been a Co-Chair of the SPIE International Conference on Signal and Image Processing for Remote Sensing since 2014. She was the Publication Chair of the International Geoscience and Remote Sensing Symposium in 2015. She has been an Associate Editor of the IEEE JOURNAL OF SELECTED TOPICS IN APPLIED EARTH OBSERVATIONS AND REMOTE SENSING since 2011 and the Guest Editor of the Special Issue on Analysis of Multitemporal Remote Sensing Data of the IEEE TRANSACTIONS ON GEOSCIENCE AND REMOTE SENSING. She is a referee for several international journals.